

RESEARCH ARTICLE | DECEMBER 18 2023

Dynamics of surfactant-laden drops in shear flow by lattice Boltzmann method

Zhe (Ashley) Chen (陈喆)  ; Peichun Amy Tsai (蔡佩君)   ; Alexandra Komrakova 



Physics of Fluids 35, 122119 (2023)
<https://doi.org/10.1063/5.0177407>



Articles You May Be Interested In

Surfactant-laden drop behavior in pore space

Physics of Fluids (January 2025)

Surfactant-laden droplet behavior on wetting solid wall with non-Newtonian fluid rheology

Physics of Fluids (September 2019)

Modeling surfactant-laden droplet dynamics by lattice Boltzmann method

Physics of Fluids (December 2020)

Dynamics of surfactant-laden drops in shear flow by lattice Boltzmann method

Cite as: Phys. Fluids 35, 122119 (2023); doi: 10.1063/5.0177407

Submitted: 21 September 2023 · Accepted: 24 November 2023 ·

Published Online: 18 December 2023



View Online



Export Citation



CrossMark

Zhe (Ashley) Chen (陈喆),  Peichun Amy Tsai (蔡佩君),  and Alexandra Komrakova 

AFFILIATIONS

Department of Mechanical Engineering, University of Alberta, Edmonton T6G 2R3, Alberta, Canada

^aElectronic mail: zhe8@ualberta.ca

^bAuthor to whom correspondence should be addressed: peichun@ualberta.ca

^cElectronic mail: komrakov@ualberta.ca

ABSTRACT

We developed and applied a diffuse interface lattice Boltzmann method for simulating immiscible liquids with soluble surfactants using a modified Ginzburg–Landau free energy functional. We first validated the approach through simulations of planar interfaces and drop equilibration in quiescent fluid. The proposed method accurately captures the phase and surfactant fields with diminishing spurious velocities of 10^{-6} . We systematically examined the effects of capillary number, comparing viscous to surface forces, the combined effect of surfactant and viscosity ratio (λ) of the drop to the continuous phase, and the bulk surfactant load on the deformation and breakage in a shear flow. At a given capillary number ($0.05 < Ca < 0.32$), drop behavior is influenced by reduced surface tension, tip-stretching, Marangoni stresses, and surface dilution. These effects either promote (by tip-stretching) or hinder (via Marangoni stresses, surface dilution) the surfactant distribution at the interface, consequently affecting the final drop morphology. As Ca increases, the competition between the viscosity ratio and the presence of surfactant determines drops' topological changes. The presence of surfactants can overcome the effect of viscosity ratio (when $0.05 \leq \lambda \leq 1.7$) and promote drop breakup, whereas highly viscous drops (either $\lambda < 0.05$ or $\lambda > 1.7$) do not break. Furthermore, high surfactant loads result in higher drop deformation and earlier drop breakup. In brief, our method successfully captures the dynamics of surfactant-laden drops in shear flow, elucidating the complex interplay between flow hydrodynamics and surfactant transport with 3D quantitative phase and surfactant concentration fields.

Published under an exclusive license by AIP Publishing. <https://doi.org/10.1063/5.0177407>

I. INTRODUCTION

Emulsions, typically composed of two or more immiscible liquids and a surfactant as a surface active agent, play a vital role in various industrial processes. Surfactants can act as an emulsifier, promoting the generation of tiny drops,¹ or a stabilizer, preventing liquid separation.² A surfactant tends to accumulate at the interface, lowering the interfacial tension between the liquids and consequently affecting the emulsion behavior.^{3,4} The generation of emulsions, i.e., the dispersion of drops of one liquid into another and their interaction with surfactants, often happens in an agitated environment, such as stirred tanks and homogenizers or microfluidics. Therefore, understanding the non-linear interplay between hydrodynamics, changes in interfacial topology, and surfactant transport is crucial for emulsion control and generation. Numerical simulation is a powerful approach that offers valuable insight into the complex interaction between these multiple phenomena. However, modeling two immiscible liquids stabilized by a soluble surfactant is challenging. Surfactant gradients give rise to varying capillary and tangential stresses. In turn, these stresses contribute

to driving forces in the flow and thus affect the distribution of surfactant.^{5–7} Numerically, a coupled system of equations needs to be solved on a continuously evolving interface,⁶ intensifying the inherent complexities of multiphase flow modeling.

A diffuse interface phase field method is widely used for simulating multiphase flows with surfactants. Rather than a sharp interface, it assumes a finite interface thickness characterized by a rapid but smooth transition in density and dynamic viscosity.⁸ The phase field variable, ϕ , differentiates the phases, evolving based on a thermodynamically consistent theory.⁹ Unlike sharp interface methods that require explicit interface reconstruction, the diffuse interface method implicitly tracks the interface, leading to reduced computational demands and simplified implementation.¹⁰ The governing equations have been solved using various numerical approaches including volume of fluid method,¹¹ front-tracking method,^{12,13} level-set method,¹⁴ and more recent mesoscale strategies such as the lattice Boltzmann method (LBM),^{3,7,15–18} which is the focus of this study.

The phase field lattice Boltzmann method has received substantial attention for its applications in multiphase flow studies. Van der Sman and van der Graaf¹⁹ used two Cahn–Hilliard-type equations to solve a binary fluid system with soluble surfactants, successfully capturing the Langmuir adsorption isotherm behavior. Later improvements by van der Sman and Meinders²⁰ generalized the free energy functional, which allows the recovery of both Langmuir and Frumkin isotherms when different bulk surfactant concentrations are presented. A similar strategy regarding the free energy functional has been applied by Liu and Zhang³ to study the effect of soluble surfactants on drop deformation, breakup, and coalescence. Both studies^{3,20} managed to recover the Frumkin adsorption, but they only present two-dimensional results with a restricted low range of surfactant concentration. Shi *et al.*¹⁵ presented an improved phase field LBM to investigate various droplet dynamics in the presence of soluble surfactant, focusing on the effect of surfactant on single drop deformation, two drops interactions, and interactions among four droplets in a shear flow. In their study, some terms in the chemical potential were neglected following the work of Yun *et al.*²¹ to restore correct interfacial behavior. These terms are also neglected in the more recent publications.^{6,7,16}

Most of the existing research on phase field LBM predominantly focuses on two-dimensional cases, considering only Langmuir adsorption isotherms and a limited range of surfactant concentrations. Furthermore, essential terms related to the surfactant concentration are often omitted from the model equations to prevent unphysical surface behavior.^{6,7,16,21} Although several phase field LB methods have been proposed for multiphase flows with surfactants, there is a compelling need to enhance these methods and develop a more comprehensive approach, contributing to a deeper understanding toward surfactant-laden drop dynamics.

In this paper, we introduce and apply a diffuse interface phase field method to conduct time-resolved three-dimensional simulations of emulsions. The underlying system of equations consists of the Navier–Stokes equations coupled with two transport equations. First, an Allen–Cahn equation governs the transport of the phase field parameter (ϕ) accounting for the two immiscible liquids and is conservative and computationally effective.²² Second, a Cahn–Hilliard equation describes the transport of the second order parameter representing the surfactant concentration (ψ). The terms of these transport equations were derived based on a free energy functional. A widely used Ginzburg–Landau functional for the pure (surfactant-free) system was modified to account for the surfactant based on prior studies.^{3,7,15,19}

The primary objective of this study is to evaluate the capability and accuracy of the proposed numerical method to characterize a surfactant-laden drop and to further analyze its response in a simple shear flow. The structure of this paper is organized as follows: Sec. II describes the mathematical methodology, followed by a comprehensive lattice Boltzmann formulation in Sec. III. Sections IV A and IV B provide validation and verification for the planar interface and circular drop cases, respectively. The behavior of surfactant-laden drops in a shear flow, considering the effects of capillary number, combined impacts of surfactant and viscosity ratio, and surfactant concentration, is detailed in Sec. IV C. Finally, conclusions are drawn in Sec. V, and the *Appendices* offer additional lattice Boltzmann formulations and benchmarks.

II. METHODOLOGY

The governing equations of a surfactant-laden emulsion include the continuity equation, the momentum equation, a conservative Allen–Cahn phase field equation, and a Cahn–Hilliard surfactant transport equation as follows:

$$\nabla \cdot \mathbf{u} = 0, \quad (1a)$$

$$\rho \left(\frac{\partial \mathbf{u}}{\partial t} + \mathbf{u} \cdot \nabla \mathbf{u} \right) = -\nabla p + \nabla \cdot \left(\mu [\nabla \mathbf{u} + (\nabla \mathbf{u})^T] \right) + \mathbf{F}_s, \quad (1b)$$

$$\frac{\partial \phi}{\partial t} + \nabla \cdot (\phi \mathbf{u}) = \nabla \cdot M_\phi \left(\nabla \phi - \frac{1 - 4(\phi - \phi_0)^2}{\xi} \frac{\nabla \phi}{|\nabla \phi|} \right), \quad (1c)$$

$$\frac{\partial \psi}{\partial t} + \nabla \cdot (\psi \mathbf{u}) = M_\psi \nabla^2 \mu_\psi. \quad (1d)$$

Equations (1a) and (1b) are the continuity and momentum equations, respectively,²³ with ρ and μ denoting fluid density and dynamic viscosity, respectively; p is the pressure, \mathbf{u} is the velocity, t denotes the time, $\mu[\nabla \mathbf{u} + (\nabla \mathbf{u})^T]$ represents the viscous stress tensor, and \mathbf{F}_s is the surface tension force. Equation (1c) is a conservative Allen–Cahn phase field equation used to capture immiscible phases.²⁴ The phase field variable ϕ has two extreme values ($\phi_b^+ = 1$ and $\phi_b^- = 0$) in the bulk phases and $\phi_0 = 0.5$ at the interface. M_ϕ characterizes the mobility of ϕ . Equation (1d) is a Cahn–Hilliard transport equation that describes the concentration of surfactant (ψ), confined between values 0 and 1, with M_ψ denoting the mobility of ψ .

The effect of two immiscible phases and surfactant is incorporated into the momentum equation via the interfacial tension force³

$$\mathbf{F}_s = -\phi \nabla \mu_\phi - \psi \nabla \mu_\psi, \quad (2)$$

which can also be expressed as $\mu_\phi \nabla \phi + \mu_\psi \nabla \psi$, by using a modified surface tension and hence modified pressure through the addition of $\phi \mu_\phi + \psi \mu_\psi$.⁷ Here, μ_ϕ and μ_ψ denote the chemical potentials of ϕ and ψ , respectively. In our approach, we adopt $\mathbf{F}_s = \mu_\phi \nabla \phi + \mu_\psi \nabla \psi$, consistent with our previous application of the surface tension force.²⁵

The capability of the current method in accurately capturing a surfactant-laden system hinges on the selection of the free energy functional, which determines the chemical potentials. For a surfactant-laden emulsion, we adapted and modified the total free energy functional (\mathcal{F}) proposed by Liu and Zhang³

$$\begin{aligned} \mathcal{F} = & \int \left[\beta \phi^2 (\phi - 1)^2 + \frac{\kappa}{2} (\nabla \phi)^2 + k_B T [\psi \ln \psi + (1 - \psi) \ln (1 - \psi)] \right. \\ & \left. + \frac{w}{2} \psi (\phi - \phi_0)^2 - \frac{d}{2} \psi (\nabla \phi)^2 - \frac{c}{2} \psi^2 - e(\phi - \phi_0)\psi \right] d\mathbf{x}. \end{aligned} \quad (3)$$

We explain each term below. The terms $\beta \phi^2 (\phi - 1)^2$ and $\frac{\kappa}{2} (\nabla \phi)^2$ stem from the Landau–Ginzburg free energy functional for a surfactant-free emulsion, representing the bulk and surface free energy, respectively.²⁶ The coefficients β and κ related to surface tension σ and interface thickness ξ of the clean system with no surfactant are given by²⁷ $\beta = \frac{12\sigma}{\xi}$ and $\kappa = \frac{3\sigma\xi}{2}$.

The Flory–Huggins potential, $k_B T [\psi \ln \psi + (1 - \psi) \ln (1 - \psi)]$, governs the entropy of surfactant-laden emulsions,¹⁹ with the product of Boltzmann constant k_B and temperature T serving as the transport coefficient for ψ transport.²⁸ Within this term, $\psi \ln \psi$ models

the ideal surfactant mixing in bulk phases with positive ψ value, while $(1 - \psi) \ln(1 - \psi)$ ensures $\psi < 1$.²⁹

On the one hand, the local coupling term, $\frac{w}{2}\psi(\phi - \phi_0)^2$, guarantees a small local surfactant concentration in the bulk phases and aids in the numerical stability of the diffuse interface model for microemulsions.³ This term should remain inactive at the interface where $\phi = \phi_0$ and reach maximum in the bulk phases.²⁹ On the other hand, the non-local coupling term, $-\frac{d}{2}\psi(\nabla\phi)^2$, accounts for the surfactants' energetic preference when absorbed at the interface.³ These terms, $-\frac{d}{2}\psi(\nabla\phi)^2$ and $\frac{w}{2}\psi(\phi - \phi_0)^2$, are complementary since the former locally attracts surfactants to the interface, while the latter penalizes the existence of free surfactants in the bulk.³⁰

The energy of the lateral interaction between two adjacent surfactants is captured by $-\frac{c}{2}\psi^2$, where $c > 0$ is assumed to express an overall attractive interaction³¹ and $c = 0$ denotes no interactions between surfactants. The asymmetric term, $e(\phi - \phi_0)\psi$, accounts for different surfactant solubilities in the bulk phases.³ If both bulk phases exhibit identical surfactant solubility, terms with coefficient e can be eliminated.³

Chemical potentials μ_ϕ and μ_ψ are derived as the variational derivatives of the free energy functional \mathcal{F} with respect to ϕ and ψ ,

$$\begin{aligned} \mu_\phi = \frac{\partial \mathcal{F}}{\partial \phi} &= 4\beta\phi(\phi - 1)(\phi - 0.5) - (\kappa - d\psi)\nabla^2\phi \\ &\quad + d\nabla\phi \cdot \nabla\psi + w(\phi - \phi_0)\psi - e\psi, \end{aligned} \quad (4a)$$

$$\begin{aligned} \mu_\psi = \frac{\partial \mathcal{F}}{\partial \psi} &= k_B T[\ln\psi - \ln(1 - \psi)] - c\psi + \frac{w}{2}(\phi - \phi_0)^2 \\ &\quad - \frac{d}{2}(\nabla\phi)^2 - e(\phi - \phi_0). \end{aligned} \quad (4b)$$

To enhance the mathematical well-posedness of the phase field method,^{6,30} we apply the same relation for the equilibrium state calculation of $\nabla\phi$ as recommended by Zong *et al.*⁷

$$|\nabla\phi| = \sqrt{\frac{2\beta}{\kappa}}\phi(1 - \phi). \quad (5)$$

Incorporating this into Eq. (4b), the chemical potential for ψ can be expressed as

$$\begin{aligned} \mu_\psi &= k_B T[\ln\psi - \ln(1 - \psi)] - c\psi + \frac{w}{2}(\phi - \phi_0)^2 \\ &\quad - \frac{d\beta}{\kappa}\phi^2(1 - \phi)^2 - e(\phi - \phi_0). \end{aligned} \quad (6)$$

The equilibrium phase field profile for an interface at location \mathbf{x}_0 is given by³²

$$\phi(x) = \frac{1}{2} \left[1 - \tanh\left(\frac{|\mathbf{x} - \mathbf{x}_0|}{\xi/2}\right) \right], \quad (7)$$

which leads to a smooth transition across the interface following the hyperbolic tangent function.

From Eq. (4b), the chemical potentials at two bulk phases $\mu_{\psi,b}^+$ and $\mu_{\psi,b}^-$ are written as

$$\begin{aligned} \mu_{\psi,b}^\pm &= k_B T[\ln\psi_b^\pm - \ln(1 - \psi_b^\pm)] + \frac{w}{2}(\phi_b^\pm - \phi_0)^2 \\ &\quad - e(\phi_b^\pm - \phi_0) - c\psi_b^\pm, \end{aligned} \quad (8)$$

where ψ_b^+ and ψ_b^- are the surfactant concentrations in the two bulk phases.

In equilibrium, $\mu_{\psi,b}^+ = \mu_{\psi,b}^-$. Equation (8) yields the surfactant concentration ratio η in the bulk phases as

$$\eta = \frac{\psi_b^+}{\psi_b^-} = \exp\left(\frac{e}{k_B T}\right) \quad (9)$$

indicating e as the determining parameter for the surfactant solubility in the bulk phases. When $e = 0$, η is 1, suggesting that the surfactant concentration is uniform in both bulk phases.

Considering $|\nabla\phi| = 1/\xi$ near the interface, the chemical potential at the interface (with $\phi_0 = 0.5$) is

$$\mu_{\psi,0} = k_B T[\ln\psi_0 - \ln(1 - \psi_0)] - c\psi_0 - \frac{d}{2\xi^2}. \quad (10)$$

The surfactant adsorption isotherm describes the relationship between the surfactant in the bulk and the surfactant adsorbed at the surface at equilibrium at a constant temperature. In the equilibrium state, $\mu_{\psi,b}^+ = \mu_{\psi,b}^- = \mu_{\psi,0}$. By balancing Eq. (10) with Eq. (8), the equilibrium surfactant adsorption isotherm can be written as

$$\psi_0 = \frac{\psi_b^+}{\psi_b^+ + (1 - \psi_b^+)\psi_c^\pm} \quad (11)$$

with

$$\psi_c^\pm = \exp\left\{-\frac{1}{k_B T}\left(\frac{w}{2}(\phi_b^\pm - \phi_0)^2 - e(\phi_b^\pm - \phi_0) + \frac{d}{2\xi^2} + c(\psi_0 - \psi_b^\pm)\right)\right\}. \quad (12)$$

The analytical equilibrium profile for the surfactant concentration at an arbitrary position \mathbf{x} can then be obtained by $\mu_{\psi,b}^+ = \mu_{\psi,0}$ at equilibrium such that

$$\psi = \frac{1}{1 + \exp\left(-\frac{\mu_{\psi,b}^{+-} - \frac{w}{2}(\phi - \phi_0)^2 + \frac{d}{2}(\nabla\phi)^2 + e(\phi - \phi_0)}{k_B T}\right)}, \quad (13)$$

where $(\nabla\phi)^2$ is calculated using the analytical ϕ distribution from Eq. (7).

The surfactant significantly reduces the interfacial tension between immiscible fluids.³³ An equation of state (EOS) defining the reduction of the interfacial tension is required. For sharp interface models, the equilibrium EOS can be derived via integration of the Gibbs equation as¹⁹

$$d\sigma = -\psi_0 d\mu_\psi. \quad (14)$$

When diffuse interface is considered, the excess surfactant concentration needs to be obtained by integration over the entire diffuse interface,³⁴ and the equilibrium EOS cannot be obtained analytically.^{3,19} Hence, van der Sman and van der Graaf¹⁹ proposed that the excess surfactant concentration at equilibrium is proportional to ψ_0 , such that³

$$d\sigma = -\alpha\psi_0 d\mu_{\psi,0}. \quad (15)$$

After substituting Eq. (10) into it, we have EOS for the diffuse interface method as

$$\sigma(\psi_0) - \sigma_0 = \alpha \left[k_B T \ln(1 - \psi_0) + \frac{c}{2} \psi_0^2 \right], \quad (16)$$

where σ_0 is the surface tension of a surfactant-free system. In the sharp interface model, $\alpha = 1$,³¹ while $\alpha \neq 1$ in the diffuse interface model. In Eq. (16), α describes the surfactant strength since a larger α means a higher surface tension reduction for a fixed surfactant concentration. For a surfactant-laden emulsion, a dimensionless number $Ex = \frac{d}{w_s^{1/2}}$ controls the amount of surfactant in the interfacial region. Therefore, altering Ex modifies the surfactant amount at the interface, influencing the surface tension reduction and the choice of α in Eq. (16).

In practice, the surface tension gradually decreases with increasing surfactant load until it reaches a certain threshold, beyond which it remains constant despite the increases in surfactant concentration. This phenomenon deviates from the continuous decrease suggested in Eq. (16) and relates to surfactants' behavior; beyond the critical micelle concentration (CMC), surfactants form micelles instead of concentrating at phase interfaces, thus surface tension stops decreasing, as confirmed by experimental observations for both liquid–liquid^{35,36} and gas–liquid³⁷ systems. In our study, we verify that the maximum surface tension decrease in each case does not exceed 50%, following the references recommendations.^{6,7}

III. LATTICE BOLTZMANN FORMULATION

A diffuse interface lattice Boltzmann method, as initially introduced by Mitchell *et al.* for the study of three-dimensional immiscible fluids,²⁷ has been expanded to include the dynamics of a soluble surfactant. This expansion is accomplished by incorporating an additional transport equation tailored to represent surfactant concentration.

In this methodology, three distinct particle distribution functions, $f_z(\mathbf{x}, t)$, $g_z(\mathbf{x}, t)$, and $h_z(\mathbf{x}, t)$, are used to solve the hydrodynamic equations, the conservative Allen–Cahn phase field equation, and the Cahn–Hilliard transport equation, respectively. These particle distribution functions represent the particle density related to a discrete lattice velocity, represented as \mathbf{e}_z , at a specific position (\mathbf{x}) and time (t). Each of these functions has an associated weighting coefficient, ω_z , which, when combined with the lattice velocity, \mathbf{e}_z , forms a velocity set defined as (\mathbf{e}_z, ω_z) .

To best replicate hydrodynamic behaviors, the distribution function f_z uses a D3Q27 lattice structure. The benefits of using this structure include enhanced isotropy, decreased spurious velocity, and increased accuracy in the model.²⁷ On the other hand, both g_z and h_z use a D3Q15 lattice structure to recover both the conservative Allen–Cahn phase field equation and the Cahn–Hilliard-like transport equation and reduce unnecessary computational cost. These lattice structures are detailed in Appendix A.

The lattice Boltzmann method (LBM) equations, when transformed to a discretized form considering variations in velocity, space, and time, are presented as follows:

$$f_z(\mathbf{x} + \mathbf{e}_z \delta t, t + \delta t) = f_z(\mathbf{x}, t) - \mathbf{M}^{-1} \hat{\mathbf{S}} \mathbf{M} [f_z(\mathbf{x}, t) - \bar{f}_z^{eq}] + F_z(\mathbf{x}, t), \quad (17a)$$

$$g_z(\mathbf{x} + \mathbf{e}_z \delta t, t + \delta t) = g_z(\mathbf{x}, t) - \frac{g_z(\mathbf{x}, t) - \bar{g}_z^{eq}(\mathbf{x}, t)}{\tau_\phi + 1/2} + F_g^\phi(\mathbf{x}, t), \quad (17b)$$

$$h_z(\mathbf{x} + \mathbf{e}_z \delta t, t + \delta t) = h_z(\mathbf{x}, t) - \frac{h_z(\mathbf{x}, t) - h_z^{eq}(\mathbf{x}, t)}{\tau_\psi}. \quad (17c)$$

For Eq. (17a), we applied a weighed multiple-relaxation-time (WMRT)³⁸ for the collision operator (shown in Appendix B). For Eqs. (17b) and (17c), a standard Bhatnagar–Gross–Krook (BGK) single-relaxation-time collision operator³⁹ is used. The relaxation time τ_ϕ is related to the mobility as $\tau_\phi = M_\phi / (c_s^2 \delta t)$.

The overall macroscopic physical variables, essential for understanding the system's behavior, are obtained from the moments of the particle distribution functions. These equations are

$$p^* = \sum_z f_z, \quad (18)$$

$$\mathbf{u} = \sum_z f_z \mathbf{e}_z + \frac{\mathbf{F}_s}{2\rho}, \quad (19)$$

$$\phi = \sum_z g_z, \quad (20)$$

$$\psi = \sum_z h_z, \quad (21)$$

where p^* is a normalized pressure calculated as

$$p^* = p / c_s^2 \rho, \quad (22)$$

and $c_s = \frac{1}{\sqrt{3}} \frac{\Delta x}{\Delta t}$ is defined as the speed of sound in LBM,⁴⁰ where Δx is the lattice spacing and Δt is the time step.

The detailed calculations for particle distributions $f_z(\mathbf{x}, t)$, $g_z(\mathbf{x}, t)$, $h_z(\mathbf{x}, t)$ and related quantities can be found in Appendix C.

IV. RESULTS AND DISCUSSION

Sections IV A and IV B preliminarily serve the purpose of validation. In Sec. IV C, we focus on new results regarding the drop deformation in shear flow. We first focus on the results of the surfactant concentration over a planar interface in Sec. IV A. Our method shows high accuracy in capturing both the Langmuir and Frumkin adsorption isotherms and captures the interface behavior with different surfactant solubilities: our numerical results in terms of interface and surfactant concentration profiles overlap with analytical solutions. We subsequently study a drop in equilibrium with soluble surfactant in Sec. IV B, illustrating the decrease in surface tension as the equation of state predicts. Finally, we present the numerical observations and discussions of the behavior of a single droplet in a simple shear flow in Sec. IV C. Throughout the analysis, we pay attention to the role of capillary number, the combined effect of viscosity ratio and surfactant, and the effect of surfactant concentration.

A. Planar interface

Focusing on surfactant concentrations across a planar interface, our results focus on three main bulk surfactant concentrations of $\psi_b = 5 \times 10^{-2}$, 1×10^{-1} , and 2×10^{-1} for both Langmuir and Frumkin adsorption isotherms.

We used pseudo-1D simulations in a domain having dimensions $L_x \times L_y \times L_z = 200 \times 4 \times 4$ lattice units. The central region, designated as $50 \leq x \leq 150$, is filled with one fluid ($\phi_b^+ = 1$), while the rest is filled with a different fluid ($\phi_b^- = 0$). All domain boundaries have periodic boundary conditions. Key properties include viscosity μ at 1/3,

surface tension σ_0 at 0.01, and several free energy functional related parameters, such as $\psi_c = 0.5$, $Ex = 0.17$, $d = \kappa$, $w = d/(Ex \cdot \xi^2)$, $e = 0$, and $c = 0$ for the Langmuir adsorption, while $c = 2k_b T$ for the Frumkin isotherm. The numerical parameters are chosen as follows: the interfacial thickness $\xi = 3$, the mobility for ψ : $M_\psi = 0.5$, and the mobility of ϕ : $M_\phi = 0.15$.

When initializing the simulation, the phase field variable ϕ is set as $\phi = 0.5$ at the interface ($x = 50$ and $x = 150$), and $\phi_b^- = 0$, $\phi_b^+ = 1$ are set in the bulk phases. Surfactant concentration ψ is initialized with a uniform value everywhere. The following procedure determines the initialized value of ψ : we first plot the surfactant concentration at equilibrium according to the analytical equilibrium solution Eq. (13) and calculate the total volume of surfactant ψ_{sum} in the domain. The initialized surfactant concentration is then calculated by $\psi_{sum}/(L_x \times L_y \times L_z)$. Note that the initialized bulk surfactant concentration would be higher than the final bulk surfactant concentration ψ_b since the surfactant accumulates at the interface when reaching equilibrium.

The results for three different bulk surfactant concentrations in terms of ϕ and ψ distribution near the interface for Langmuir and Frumkin isotherms are plotted in Fig. 1. The numerical results agree well with the analytical solution for ϕ and ψ . The interface behavior depicted by our model aligns well with analytical solutions, indicating the accuracy of our simulations. Several researchers mentioned that considering the terms involving ψ in chemical potential calculation Eq. (4a) ($(d\psi/\nabla^2\phi + d\nabla\phi \cdot \nabla\psi + w(\phi - \phi_0)\psi - e\psi$ in our case) leads to unphysical surface behavior^{7,21} such as interface broadening or interface location shifting. In our method, we used the Allen-Cahn phase field equation [Eq. (1c)], kept these terms, and found that the ϕ profile does not display these unphysical surface effects.

For lower surfactant concentration in the bulk, ψ profiles corresponding to two different adsorption isotherms overlap. Yet, differences emerge as the bulk surfactant concentration increases, in line with Liu and Zhang's findings,³ suggesting that the Frumkin adsorption considering surfactant particle interactions is more applicable than the Langmuir adsorption for higher bulk concentration. Therefore, we consider only the Frumkin adsorption isotherm for the rest of the cases. We also observed an asymmetry of ψ when $\psi_b = 0.2$ and $\psi_o \approx 0.6$. This is because the chemical potential for ψ is sensitive for high local ψ values, according to Eq. (4b); thus, a small deviation can lead to the asymmetry of ψ . Regardless, the results for the ϕ and ψ fields remain stable throughout our observation.

Next, we examine the influence of interfacial thickness, ξ , on the simulation results. Figure 2 shows the ψ distribution over the interface for varying ξ values. For $\xi = 2$, ψ distribution mismatches the analytical solution; the maximum value of ψ is not at the interface, suggesting inaccurate results. As ξ increases, ψ distribution over the interface can be well captured; larger values of ξ better match the analytical solutions, especially for ψ_o . To balance the model accuracy and computational time, $\xi = 3$ is used for subsequent simulations.

Using the same simulation parameters, we further investigate the planar interface equilibrium profile when subjected to different surfactant solubilities in the bulk phases. We set the bulk surfactant concentration $\psi_b = 0.05$ and explored the coefficient e , which governs the solubility ratio between the bulk phases. Specifically, we analyzed the values of $e = 0, 0.002$, and 0.004 .

The surfactant preferably dissolves in the central region ($50 \leq x \leq 150$, $\phi = 1$). Consequently, the solubility ratio between the

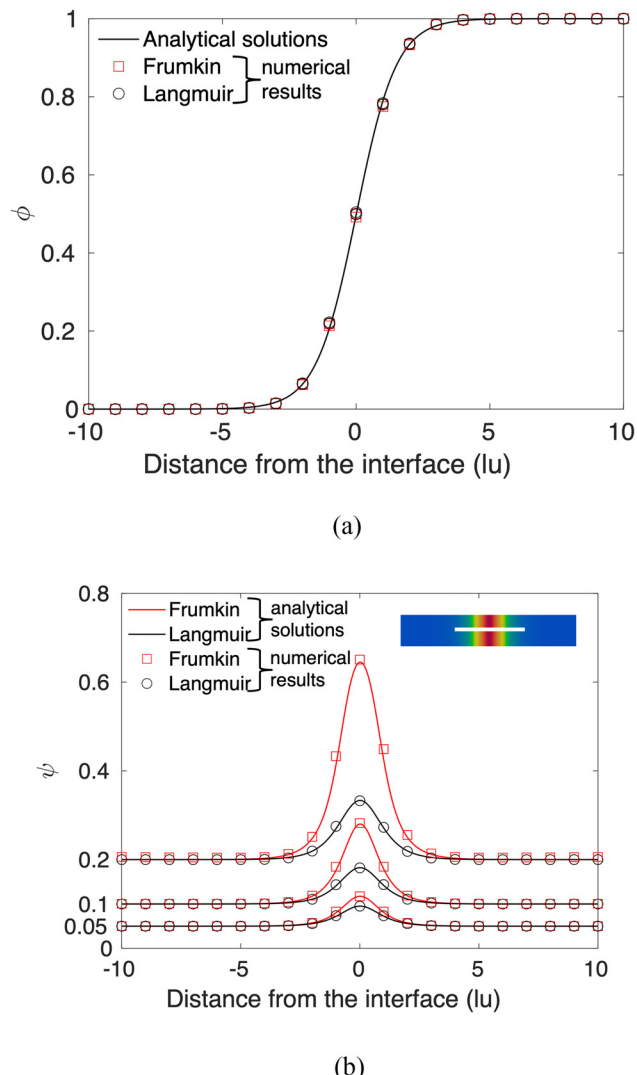


FIG. 1. Profiles of (a) the order parameter, ϕ , and (b) the surfactant concentration, ψ , for a plane near the interface. Square and circle symbols represent our numerical results for Langmuir (with $c = 0$) and Frumkin adsorption isotherms (using $c = 2k_b T$), respectively. The red and black curves are the corresponding analytical solutions.

two bulk phases, represented as $\eta = \psi_b^+/\psi_b^- = \exp\left(\frac{e}{k_b T}\right)$, yields values of 1, 1.58, and 3.5, according to Eq. (9). The results of ϕ and ψ profiles along the interface are presented in Fig. 3. The numerical results of the phase field agree well with the analytical results, and the interface behavior is unaffected by different surfactant concentrations in the two bulk phases.

To analyze ψ , we dimensionalized the y axis to represent the local to bulk surfactant concentration ratio in the less preferably dissolved phase, denoted as ψ/ψ^- . The results agree well with the analytical solutions; the surfactant reveals different solubilities in two bulk phases, with a peak at the interface. A noteworthy observation is that varying the parameter e predominantly influenced the solubility ratio across

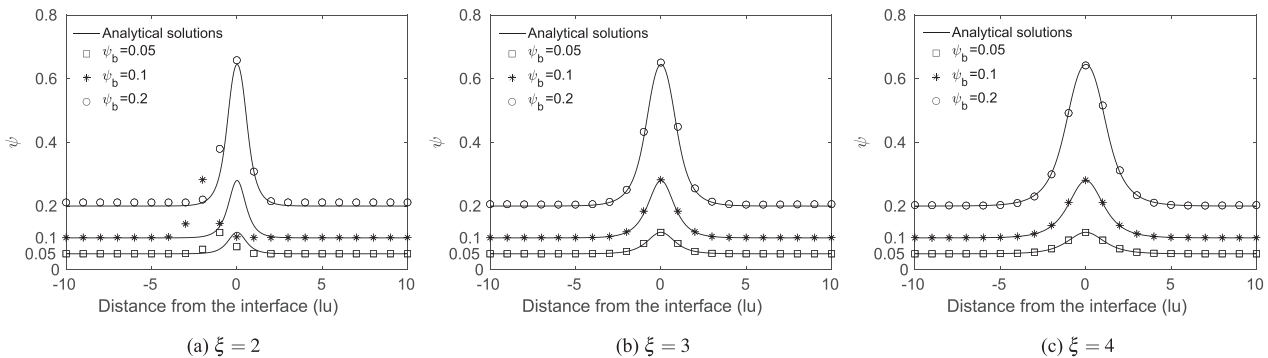


FIG. 2. Profile of the surfactant concentration near the interface with different ζ . The solid lines are the analytical solutions, and the symbols are the numerical results.

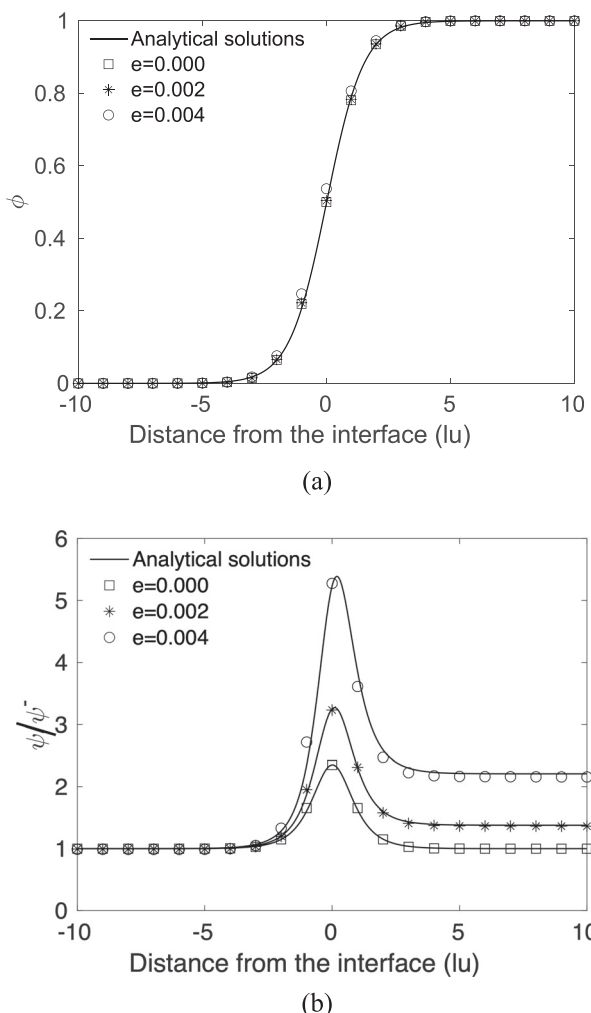


FIG. 3. (a) Profiles of the phase identifier ϕ for different values of e near the interface. (b) Profile of the surfactant concentration near the interface, with the y axis being the ratio of local surfactant concentration vs its solubility in the less favorably dissolved phase ψ/ψ^- . Square symbols represent numerical results, and black solid lines are the corresponding analytical solutions.

phases without affecting the overall surfactant quantity. This infers that, given a certain amount of surfactant in the domain, manipulating e can alter the soluble surfactant distribution across the bulk phases. An increased value of e leads to a higher ψ_0 at the interface, meaning that ψ_b^+ and ψ_b^- are comparably lower than the cases with low e values because ψ is conserved. For subsequent simulations, we consider only when the bulk surfactant concentration remained uniform (i.e., $e = 0$).

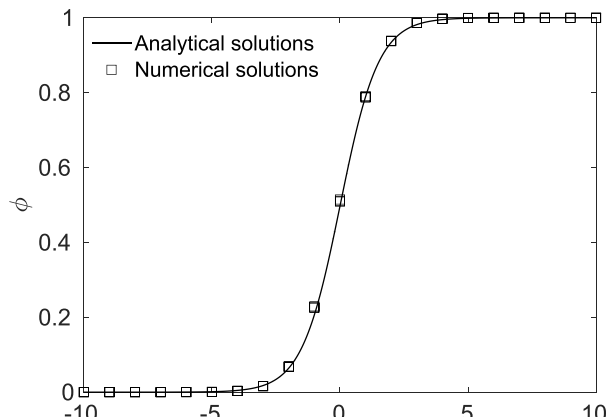
In summary, when applied to a planar interface, our proposed method shows great accuracy in capturing both the Langmuir and Frumkin adsorption isotherms. Additionally, it proves proficient in modeling emulsion with different surfactant solubilities, making the method suitable when compared to experimental results and representing realistic systems since surfactants normally display different solubilities in bulks.

B. Drop equilibration

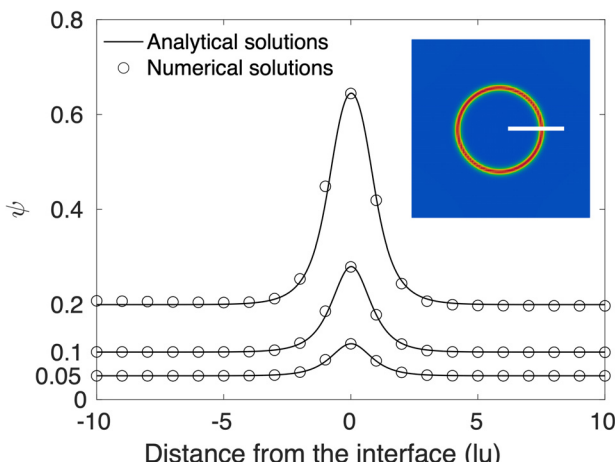
This section is dedicated to a benchmarking analysis of a spherical drop undergoing equilibration for a surfactant-laden multiphase system. Initially, a droplet with a radius of $R_0 = 20$ is placed at the center of the computational domain of $L_x \times L_y \times L_z = 80 \times 80 \times 80$ with the periodic boundary conditions in all directions. The key properties and numerical parameters include: surface tension $\sigma_0 = 0.01$, interfacial thickness $\xi = 3$, mobility for ψ designated as $M_\psi = 0.5$, and for ϕ , $M_\phi = 0.15$. We embarked on understanding the droplet's equilibrium state under varied bulk surfactant concentrations, specifically $\psi_b = \{5 \times 10^{-2}, 1 \times 10^{-1}, 2 \times 10^{-1}\}$.

The phase field variable at equilibrium at the plane of $z = 40$ is shown in Fig. 4(a), and the corresponding surfactant concentration is shown in Fig. 4(b), where the symbols represent the numerical results and the black curves represent the analytical solutions. The maximum deviation between the numerical and analytical results from Eq. (11) is 4.7% for ψ when $\psi_b = 0.2$, which confirms that our method can accurately simulate a high surfactant load at the interface.

To test the anisotropy of the field, the mean and standard deviation of ϕ and ψ and their gradients were calculated at various distances (binned on the scale of 0.1 lattice units; the value between grids is achieved by linear interpolation) from the droplet center.⁴¹ Figure 5(a) shows the results of the phase variable ϕ for $\psi_b = 0.05$, and Fig. 5(b) shows the corresponding results of ψ . The true interface location (where $\phi = 0.5$ and ψ is at maximum) is marked as a black vertical



(a)



(b)

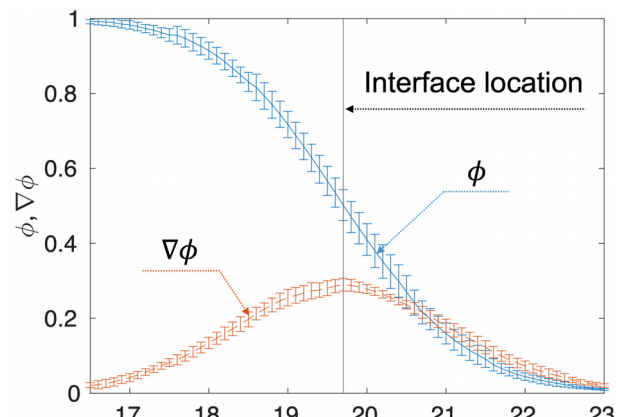
FIG. 4. Profiles of (a) the order parameter, ϕ , and (b) the surfactant concentration, ψ , for a drop near the interface. The symbols represent the numerical results, and black solid lines are the corresponding analytical solutions for $\psi_b = \{5 \times 10^{-2}, 1 \times 10^{-1}, 2 \times 10^{-1}\}$.

line. Our results indicate that the true interface location is around 19.7 from the drop interface, which is slightly smaller than $R_0 = 20$. The three-dimensional phase field is not a perfect spherical shape, and the numerical results for ψ are not in perfect symmetry across the interface. Overall, our results showed an acceptable anisotropy, proving the stability and accuracy of the method.

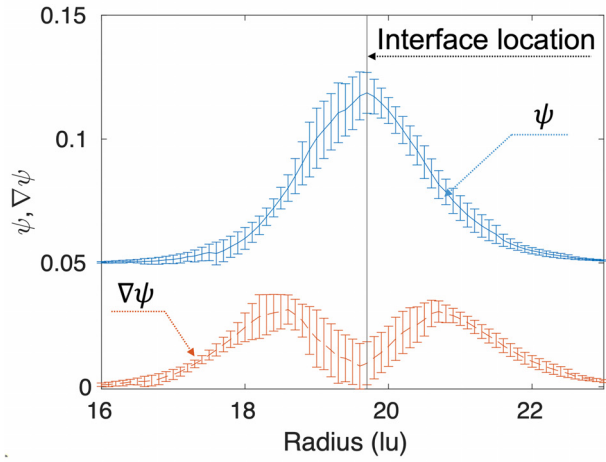
In addition, this benchmark serves as a platform for studying the reduction of surface tension. Upon system equilibration, the surface tension σ can be calculated using the Laplace law⁴²

$$\Delta p = p_A - p_B = \frac{2\sigma}{R_0}, \quad (23)$$

where p_A and p_B are the pressure values inside and outside of the drop, respectively, as determined by Eq. (22).



(a)



(b)

FIG. 5. (a) Interface profile ϕ and gradient profile $\nabla\phi$ at circular droplet equilibration. (b) Surfactant concentration ψ and gradient profile $\nabla\psi$ at circular droplet equilibration: data have been collected in bins of width 0.1 lattice spacings, and the error bars are one standard deviation.

Introducing a surfactant into the system results in a subsequent decrease in surface tension by $\Delta\sigma/\sigma_0$. Figure 6(a) illustrates the relationship between $\Delta\sigma/\sigma_0$ and interface surfactant concentration $\ln(1 - \psi_0)$. Generally, the surface tension can be systematically 10%–15% smaller than the theoretical input values because the narrow interface leads to inaccuracies in gradient calculations.⁴¹ To eliminate this numerical deviation and obtain the true surface tension, we use the decreased σ in the pure system as the initial σ_0 . The numerically predicted value of the surface tension of the pure system σ_0 , instead of the initial input of 0.01, was calculated using a surfactant-free system under the same conditions and measured as 0.008 89.

In Fig. 6(a), the numerical results (symbols) agree well with the analytical solution (solid curves) by fitting $\alpha = 0.9806$ to Eq. (16). The decreasing trend of surface tension matches well with EOS, and a higher surfactant load leads to a higher reduction.

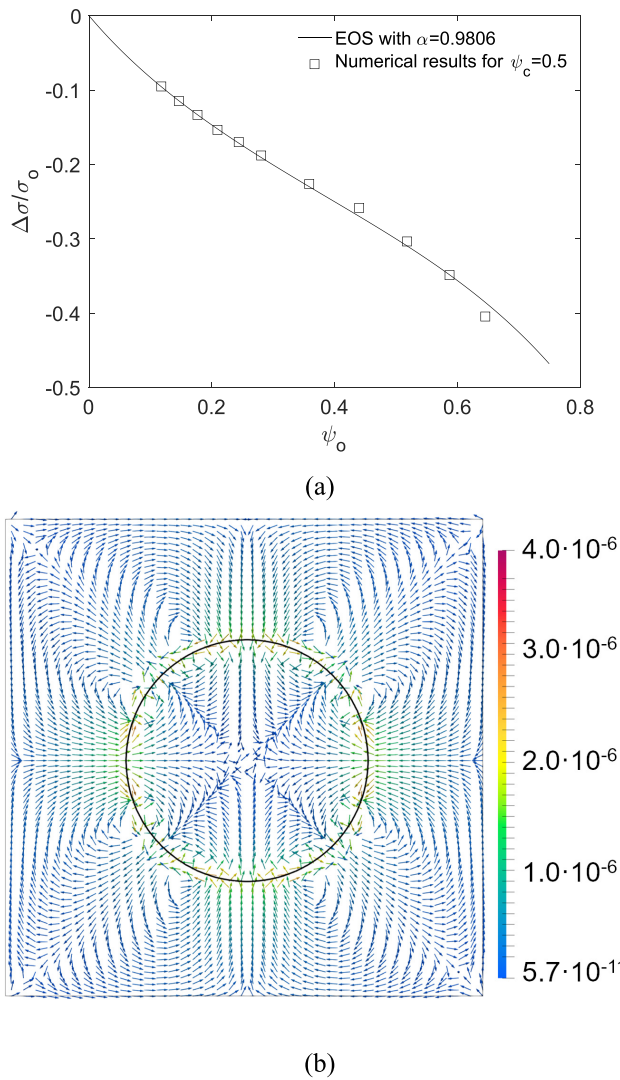


FIG. 6. (a) The decrease in normalized surface tension $\Delta\sigma/\sigma_0$ as a function of surfactant concentration at the interface ψ_0 for different surfactant loads. The analytical solutions are plotted with solid line with $\alpha = 0.9806$. (b) Spurious velocity around the drop interface: the arrows are the velocity vectors, and the black line represent the drop surface.

Parasitic currents around the interface are a numerical artifact in many numerical approaches and should be eliminated.^{43–45} In our simulation, as shown in Fig. 6(b), the maximum spurious velocities $|u_{max}| = (\sqrt{u_x^2 + u_y^2 + u_z^2})$ observed are approximately 10^{-6} , revealing good accuracy of the numerical method.

C. Drop deformation in a simple shear flow

In this section, we elucidate the numerical results concerning the behavior of a single droplet in a simple shear flow. Section IV C 1 describes the simulations of the pure system without a surfactant to identify the choice of numerical parameters. These

parameters are then used consistently in the following simulations involving a surfactant-laden drop. In Sec. IV C 2, the impact of capillary number on drop deformation in creeping flow is analyzed. In particular, the addition of surfactants results in enhanced drop deformation. Several factors, including surface tension reduction, tip-stretching, Marangoni, and surface dilution effects, affect this deformation. While the surfactant induces droplet deformation, the viscosity ratio acts contrarily, hindering the deformation. We found that the presence of surfactant can overcome the effect of the viscosity ratio within a certain range, consequently decreasing the critical capillary number, above which the drop develops an end-pinch mechanism and breaks.⁴⁶ The influence of surfactant concentration is further discussed in Sec. IV C 4, where a higher surfactant concentration leads to larger drop deformation and faster drop breakage.

In the simulations described herein, a drop (fluid 1) is centrally placed within the domain and is surrounded by fluid 2 as the bulk fluid. The domain is periodic in the x -direction and has no-slip boundary conditions at the walls, which are bounce-back conditions in LBM. A shear flow, characterized by the shear rate $G = 2v/H$, is introduced by moving the domain's top and bottom walls in opposite directions, as shown in Fig. 7(a). In the absence of surfactant, the key dimensionless controlling parameters include

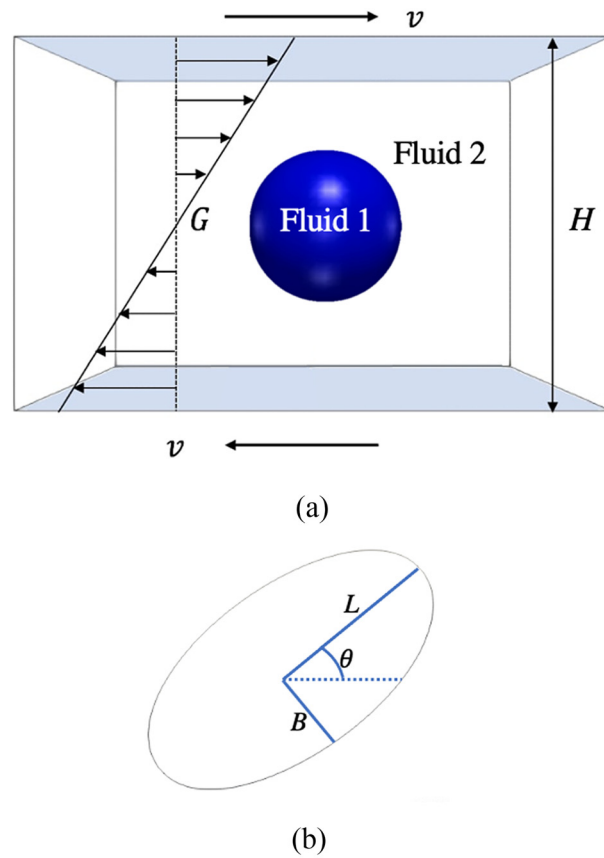


FIG. 7. (a) Simulation domain for a single drop in a simple shear flow. (b) The schematics of Taylor deformation parameter, D_T , and inclination angle, θ .

Reynolds number Re , capillary number, Ca , and viscosity ratio between the phases, λ ,^{42,47}

$$Re = \frac{\rho G R_0^2}{\mu_c}, \quad Ca = \frac{\mu_c G R_0}{\sigma_0}, \quad \lambda = \frac{\mu_d}{\mu_c}, \quad (24)$$

where ρ is the density, μ_c and μ_d are the dynamic viscosity of the continuous liquid and dispersed phase, respectively, σ_0 is the surface tension for the pure system (before adding the surfactant), and R_0 is the radius of the drop.

To quantify drop deformation, the Taylor deformation parameter D_T is used^{48,49}

$$D_T = \frac{L - B}{L + B}, \quad (25)$$

where L and B are the lengths of the major and minor axes of the deformed droplet, respectively, as shown in Fig. 7(b). The inclination angle θ , formed by the droplet's major axis with the x axis, characterizes the degree of the droplet's inclination.

1. LBM numerical parameters

The lattice Boltzmann method requires an explicit specification of several numerical parameters, notably interface thickness ξ , mobility M , and relaxation time τ . Two dimensionless parameters are introduced to characterize the additional degrees of freedom related to the numerical technique: the Cahn number, which is the interface thickness to drop radius ratio⁵⁰

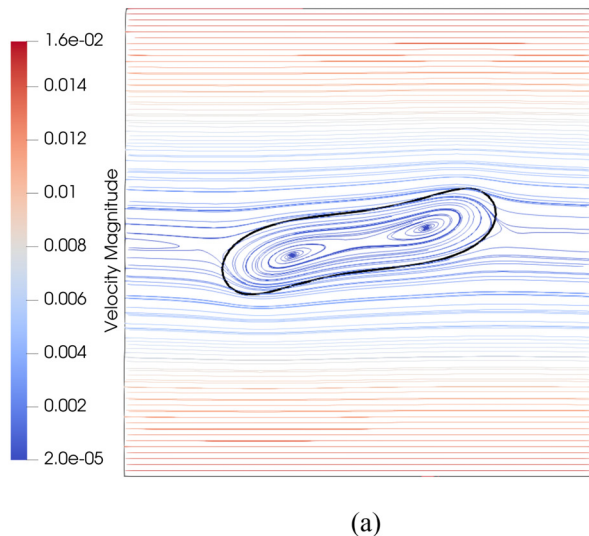
$$Ch = \frac{\xi}{R_0} \quad (26)$$

and the interface Peclet number, defined as the timescale ratio of convection to interface diffusion²⁷

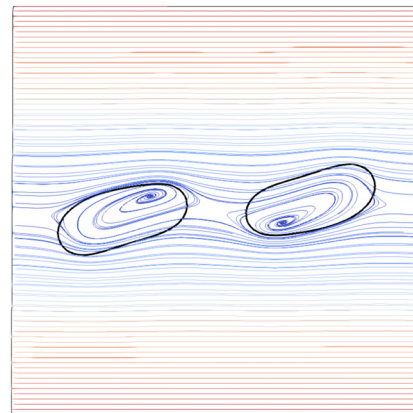
$$Pe = \frac{G R_0 \xi}{M_\phi}. \quad (27)$$

A surfactant-free emulsion system is essentially governed by three physical dimensionless numbers (Re , Ca , λ) and two numerical parameters (Ch , Pe). It is imperative to carefully select these numbers to accurately capture the drop behavior at given physical dimensionless numbers. To this end, we performed a series of simulations of a pure system at $Re = 0.0625$, $Ca = 0.45$, $\lambda = 1$, numerical parameters were tested on $\xi = 2, 3, 4$ and $M_\phi = 0.15, 0.75, 1.5$ so that $Ch = 0.1, 0.15, 0.2$ and $Pe = 0.0826, 0.016452, 0.00826$. To avoid the wall effect, the domain has a size of $L_x \times L_y \times L_z = 8R_0 \times 8R_0 \times 4R_0$ following the recommendation by Komrakova *et al.*,⁴⁷ and the drop radius $R_0 = 20$. We methodically examine the influence of the Peclet and Cahn numbers (see Appendix D), summarizing that smaller Cahn numbers and larger Peclet numbers promote drop deformation. However, unstable results are obtained when the Peclet or Cahn numbers are too small, e.g., $Pe \leq 0.00826$ or $Ch \leq 0.1$. Through detailed comparison, we chose the optimal numerical parameters to be $\xi = 3$ and $M_\phi = 0.15$, when $Ch = 0.15$ and $Pe = 0.0826$.

To further validate these parameters, we set the parameter values close to the critical capillary number ($Ca_c = 0.41$)⁴⁶ and performed two cases for $Ca = 0.4$ and $Ca = 0.42$. The results are given in Fig. 8, revealing that the drop reaches a stable shape at



(a)



(b)

FIG. 8. LB simulation results of pure drop shape (black curve stands for the interface) and streamlines in the x - y plane at $z = L_z/2$ for (a) $Ca = 0.4$ and (b) $Ca = 0.42$ at $Pe = 0.0826$ and $Ch = 0.15$.

equilibrium at $Ca = 0.4$, while it breaks for $Ca = 0.42$. Since the drop breakage behavior is well captured, this validated numerical parameter set is subsequently used in all surfactant-laden drop simulations.

Several simulations leading to stable drop deformation (no breakage) have been performed and quantitatively compared with benchmark data at different Re and Ca . Detailed results are presented in Appendix E, showing excellent agreement with existing reference data.

2. The effect of capillary number

We started our study by examining the influence of capillary number on drop deformation in creeping flow. The final shape of a surfactant-free drop in a shear flow is determined by the

competition between the viscous and surface tension forces.⁶ Viscous forces elongate the droplet, whereas surface tension forces restore the spherical shape. This balance is characterized by the capillary number. An established analytical solution for the Taylor deformation parameter D_T for a surfactant-free drop in creeping flow is given by^{49,51}

$$D_T = \frac{35}{32} Ca \left[1 + C_{SH} \frac{3.5}{2} \left(\frac{R_0}{H} \right)^3 \right], \quad (28)$$

with C_{SH} being a numerical coefficient equal to 5.6996.⁵¹

When a surfactant is added, the surface tension decreases which needs to be accounted for in the calculation. To quantitatively compare the results for a surfactant-laden drop deformation obtained against the analytic relation,^{49,51} an effective capillary number is used

$$Ca_e = \frac{\mu_c G R_0}{\sigma_{\text{true}}}, \quad (29)$$

where σ_{true} is the true surface tension after adding the surfactant. σ_{true} can be obtained from a static case where no motion is applied, as shown in Fig. 6(a). By inserting $Ca_e = (\sigma_0/\sigma_{\text{true}})Ca$ in Eq. (28), we have the analytical solution for surfactant-laden drop as

$$D_T = \frac{35}{32} Ca \frac{\sigma_0}{\sigma_{\text{true}}} \left[1 + C_{SH} \frac{3.5}{2} \left(\frac{R_0}{H} \right)^3 \right]. \quad (30)$$

We study the deformation of pure and surfactant-laden drops in a shear flow for different capillary numbers ($0.05 - 0.32$). We keep $\lambda = 1$, $Re = 0.0625$ for both emulsions, and the bulk surfactant load is $\psi_b = 0.1$ when the surfactant is presented. Other parameters are chosen as: $\sigma_0 = 0.01$, $\xi = 3$, $\tau_g = 1$, $M_\phi = 0.15$, and $M_\psi = 0.5$. Domain

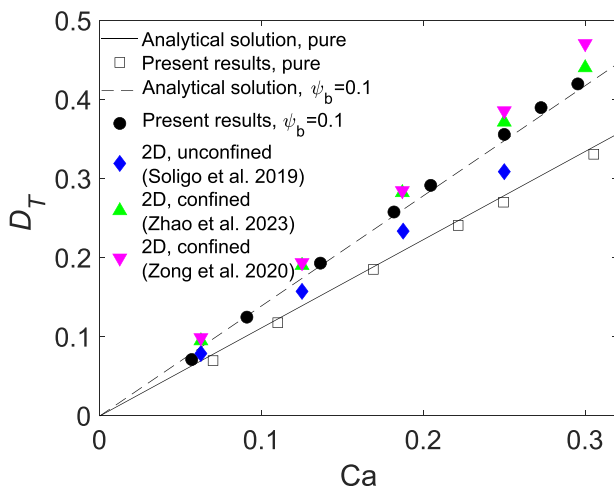


FIG. 9. Analytical solutions and numerical results for deformation parameter D_T in pure system and $\psi_b = 0.1$ at different capillary numbers.

size is $L_x \times L_y \times L_z = 8R_0 \times 8R_0 \times 4R_0$. Modifications to the capillary number were made by changing the shear rate and viscosity of the continuous phase.

The deformation parameter D_T for pure and surfactant-laden under shear is presented in Fig. 9. The numerical results agree well with the analytical solutions for the pure system, with the maximum deviation between them being $\approx 2.9\%$ at $Ca = 0.32$. When a surfactant is added, the drop deforms more, and the drop deformation parameter increases linearly with increasing capillary number, with a maximum deviation 2.7% at $Ca = 0.32$. In Fig. 9, we also include relevant numerical results of surfactant-laden drops in two-dimensional confined^{17,16} and unconfined⁶ channels. Consistent trends are found despite different simulation domains and surfactant isotherms are considered.

Figure 9 shows that the surfactant-laden drops undergo greater deformation than their pure counterparts at equivalent Ca . This enhanced deformation is attributed to a surfactant-induced reduction in surface tension, resulting in greater capillary numbers. We compare the drop deformation for both cases under the same effective capillary number to study whether reduced surface tension is the sole cause for the deviation between pure and surfactant-laden drop deformations. We performed an additional series of pure drop simulations, with the initial σ_0 equal to σ_{true} for a given set of flow conditions. According to Fig. 6(a), surface tension has a 16.7% reduction when surfactant load $\psi_b = 0.1$ is presented. σ_0 for pure simulations is carefully chosen to match the reduction and achieve identical capillary numbers with surfactant-laden drops.

The numerical results of the Taylor deformation parameter and the inclination angle for two scenarios (with and without surfactant) at the same Ca_e are presented in Fig. 10. The shape of the pure (with $\sigma_0 = 0.0081$) and surfactant-laden drops under various Ca_e values ($Ca_e = 0.072, 0.249, 0.305$, and 0.361) are also presented in Fig. 10. In both scenarios, drop deformation increases with increasing Ca_e , while the inclination angle decreases with the increase in Ca_e . For small Ca_e , the difference in deformation between pure and surfactant-laden drops is negligible, consistent with experimental observations.⁵² As Ca_e increases, the presence of surfactant promotes drop deformation and rotation, compared to pure drop. This suggests that the surfactant reduces surface tension σ and causes more physical phenomena. Following the discussions of Liu and Zhang,³ we elaborate on additional physics stemming from surfactants; the difference in the drop shape between surfactant-laden and pure drops at high Ca numbers originates from the non-uniform distribution of surfactant at the interface [shown in Fig. 11(a)]. In Fig. 11(b), the maximum ψ location is marked in red, and the minimum ψ location is marked in blue. The non-uniform distribution of surfactant contributes to three different effects: tip-stretching, Marangoni, and surface dilution. These effects, previously identified by Hu and Lips⁵² for insoluble surfactants based on an experimental study, serve as the framework to elucidate our findings.

As shown in Fig. 11(a), the surfactant accumulates at the tips of the drop due to the transport of the surfactant, leading to a local decrease in surface tension and stretched tips compared to pure drops. This effect is called tip-stretching,⁵² which promotes drop deformation. As observed from the drop shape comparisons in Fig. 10, the

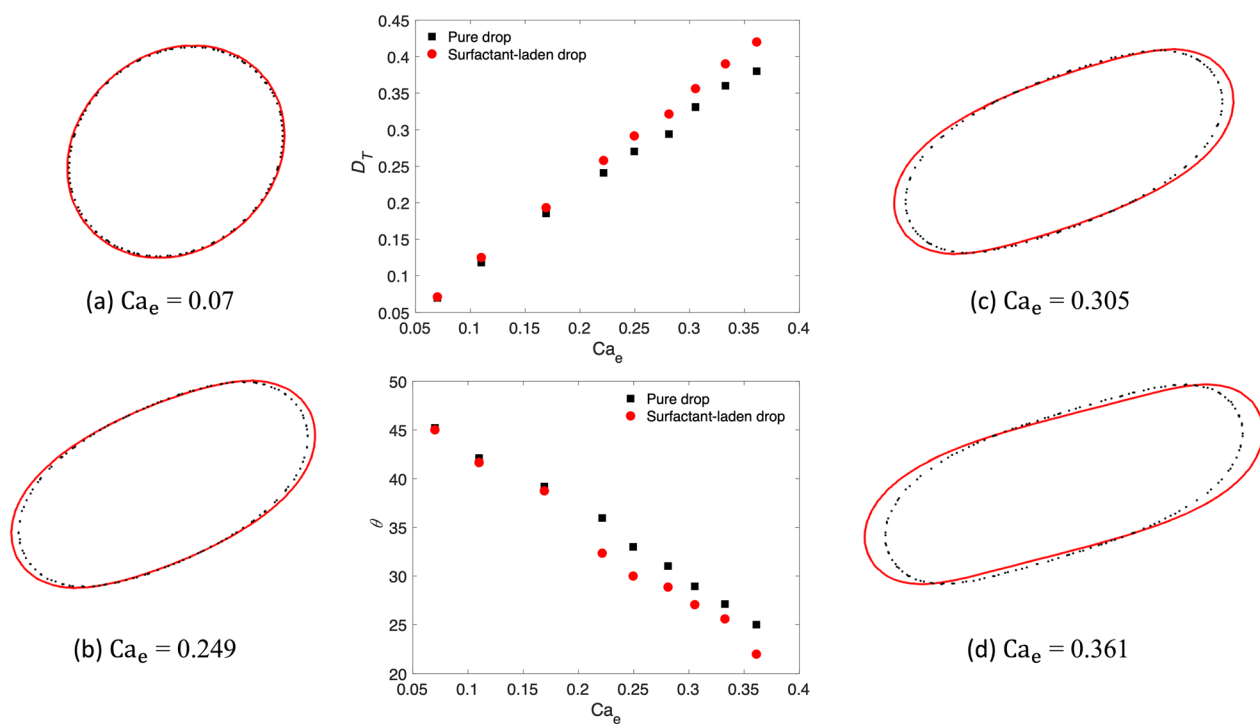


FIG. 10. Comparison between surfactant-laden and pure drops at the same Ca_e . In the center, the red and black symbols represent the surfactant-laden drop and the pure drop, respectively. On the side, the drop shape at different Ca_e is presented, with black solid (dashed) lines for surfactant-laden (pure) drops.

03 June 2023 09:13:30

surfactant-laden drop is more elongated and stretched near the drop tip than the belly.

The Marangoni force, \mathbf{F}_M , arises from the surface tension gradient and can be calculated as the tangential component of the surface tension force \mathbf{F}_s (Ref. 53) at the drop interface as

$$\mathbf{F}_M = (\mathbf{I} - \mathbf{n} \otimes \mathbf{n}) \cdot \mathbf{F}_s. \quad (31)$$

Here, \mathbf{I} is the identity tensor, and \mathbf{n} is the normal to the drop surface. We normalize the magnitude of the local Marangoni force by its maximum value $F^* = |\mathbf{F}_M|/|\mathbf{F}_M|_{max}$. The three-dimensional visualization of the normalized Marangoni force F^* at $Ca_e = 0.305$ is shown in Fig. 12. Marangoni force acts from the drop tip toward the drop belly, hindering the continuous movement of the surfactant to the tip. An increase in Ca_e amplifies the Marangoni force due to a larger surface tension gradient. As a result, the Marangoni force tends to decrease the non-uniform surfactant distribution, which leads to a reduced surface tension gradient and, subsequently, lessen drop deformation.

During deformation, an expansion of the drop's surface area dilutes the average surfactant concentration on the surface, thus enhancing the surface tension and reducing deformation—a phenomenon termed the “surface dilution effect.” To quantify this, we calculate the average surfactant load at the interface by dividing the total surfactant load at the surface $\psi_{surface}$ by the surface area S_{drop} at different effective capillary numbers, while $\psi_{surface}$ is

calculated from the numerical equilibrated ψ distribution. The outcomes of this simulation are shown in Fig. 13. The average surfactant load at the interface decreases rapidly at high Ca_e values, suggesting a reduced overall impact of surfactant on the drop. Therefore, the surface dilution effect increases significantly with high Ca_e and hinders drop deformation.

Coupling with the aforementioned effects, we discuss the non-uniformity of the surfactant at the interface using a dimensionless surfactant concentration $\psi^* = \psi/\psi_0$,¹⁶ where ψ_0 is the initial value of the surfactant concentration at the interface. Figure 14 shows the maximum and minimum of ψ^* at the interface after the drop reaches equilibrium with varying Ca_e .

The non-uniformity of the surfactant concentration increases with the capillary number when it is relatively small ($Ca_e < 0.1$). As the capillary number increases, the inhomogeneity tends to stabilize ($0.1 < Ca_e < 0.3$). When the capillary number is high ($0.3 < Ca_e < 0.36$), ψ_{max}^* slightly decreases and so does the inhomogeneity. We categorize the surfactant concentration variation into three distinct regions based on this behavior.

The behavior of ψ can be explained as follows: in regime I, at $Ca_e < 0.1$, the inhomogeneity of the surfactant is small, and the drop does not feel its effect other than reduced surface tension, therefore surfactant-laden drops behaves the same as pure drops with same Ca_e , as shown in Fig. 10(a). As Ca increases within $0.1 < Ca_e < 0.3$ (regime II), the surfactant inhomogeneity continuously increases, and the surfactant accumulates more at the drop tips. Subsequently, the

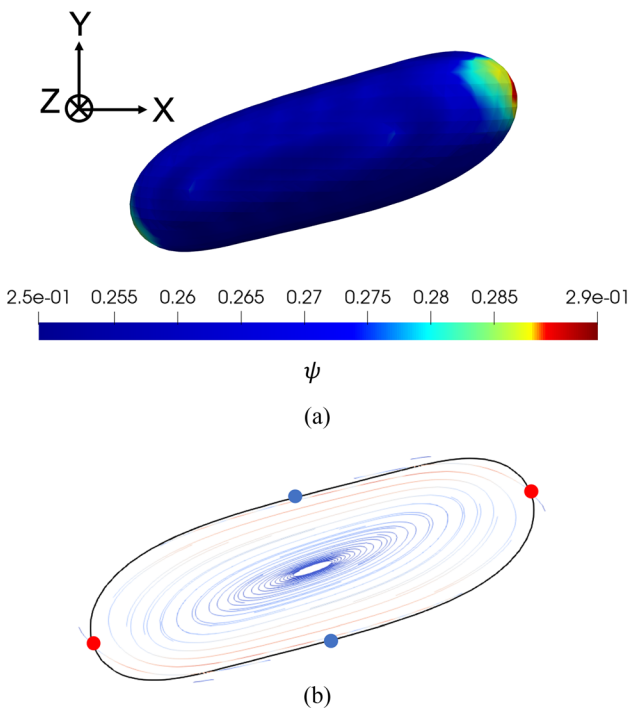


FIG. 11. Drop equilibrium at $Ca_e = 0.361$, $Ca = 0.26$, $Re = 0.0625$, $\lambda = 1$ (a): three-dimensional ψ field at the drop interface; (b) black curves represent the drop shape; the streamlines are colored by the velocity magnitude; the maximum and the minimum surfactant concentration locations are marked by red and blue bullets, respectively.

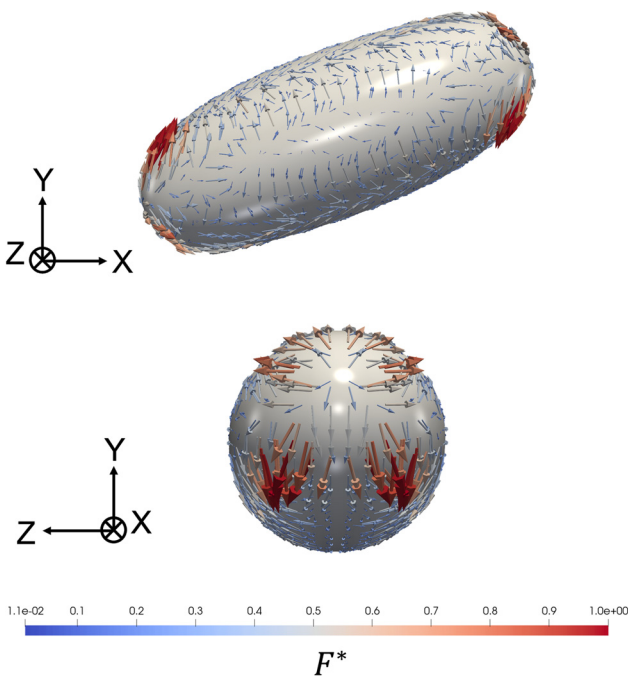


FIG. 12. Marangoni force at the interface of a drop for $Ca_e = 0.305$: front view (top) and right view (bottom). Arrows are the normalized Marangoni forces F^* .

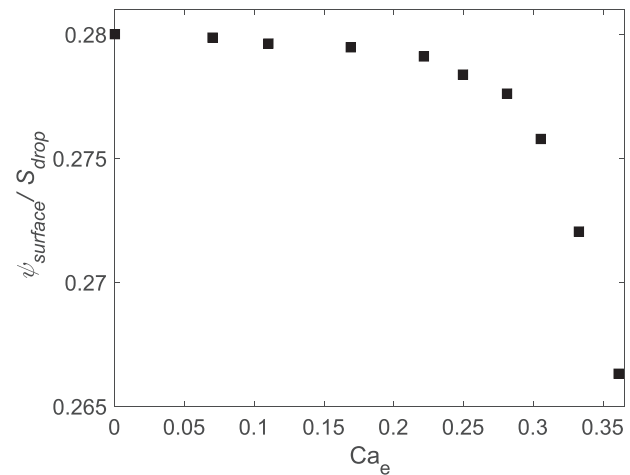


FIG. 13. Average surfactant load at interface at different effective capillary numbers.

high surfactant concentration creates local low surface tension zone around the tips, making the drop more prone to elongation, known as the tip-stretching effect [see Figs. 10(b) and 10(c)]. When the capillary number is high at $0.3 < Ca_e < 0.36$ (regime III), the increase in surfactant inhomogeneity and surface area results in higher Marangoni and surface dilution effects, which would prevent further aggregation of the surfactant to the droplet tip. The non-uniformity of the surfactant at the interface decreases after reaching its maximum (at approximately $Ca_e = 0.28$).

In summary, surface tension reduction, tip-stretching, Marangoni, and surface dilution effects govern the surfactant-laden drop behavior in a creeping flow. However, with a different surfactant these effects can be less or more dominant at specific Ca_e . Therefore, such classification with specific critical

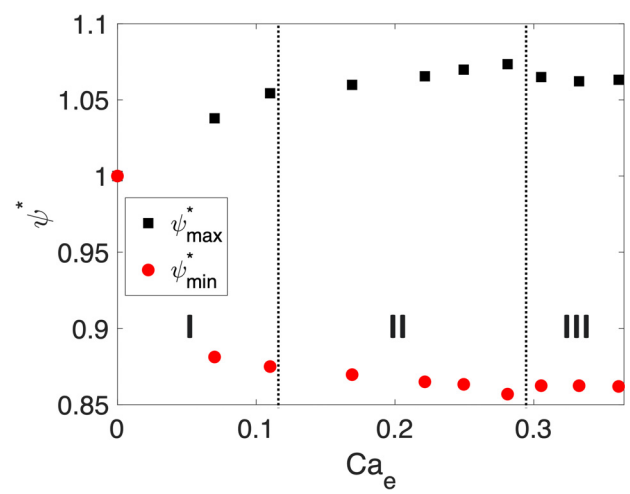


FIG. 14. Dimensionless surfactant concentration ψ^* for $Re = 0.0625$ and $\lambda = 1$ at different effective capillary numbers, Ca_e .

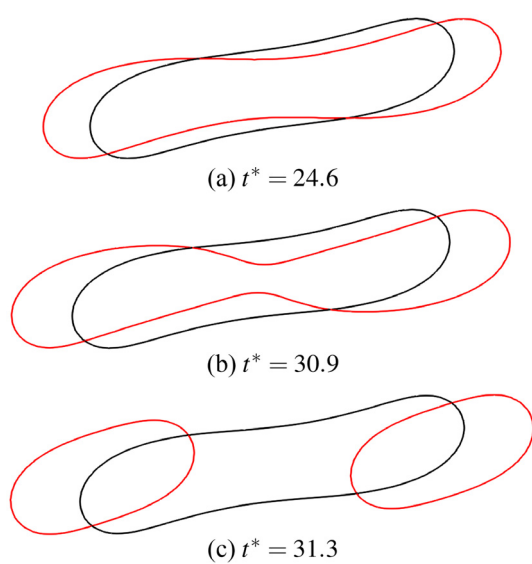


FIG. 15. The snapshots of the drop shape at different time instances for $\lambda = 1$; $Re = 0.0625$; $Ca = 0.40$. The black curves represent pure drops, and the red curves represent surfactant-laden drops with $\psi_b = 0.1$.

values of Ca_e delineating different regimes may change for different surfactant type, adsorption isotherm (the ratio of ψ_b/ψ_0), and concentration (ψ_b value).

3. Combined effect of viscosity ratio and surfactant

The capability of our model to accurately simulate a system with varied viscosity ratios was confirmed in our previous publications.^{25,54} In addition, the benchmarks for the surfactant-free drop with viscosity ratios at $Ca = 0.28$ and $Ca = 0.3$ are provided in Appendix F. Specifically, we captured the drop breakage near the critical capillary number when the viscosity ratio, λ , was 2.

In a system with $Re = 0.0625$, $Ca = 0.32$, $\psi_b = 0.1$, and $\lambda = 1$, the effective capillary number is $Ca_e = 0.40$. This value is slightly lower than the critical capillary (~ 0.41) for a pure system. Under this condition, surfactant-laden drop breaks (red curves) while pure drop (black curves) remains stable, as shown in Fig. 15. The timescale t^* is calculated as $t^* = tG$, where t is the time steps and G is the shear rate. This proves that the presence of surfactant promotes drop deformation and breakup.

The increase in the viscosity ratio between the phases prevents drop deformation and keeps the drop stable.⁵⁵ Consequently, the presence of surfactant and the increase in viscosity ratio exhibit opposing effects on drop deformation and breakup. To understand the synergistic effect of both viscosity ratio and surfactant, we simulated surfactant-laden drops with different viscosity ratios at $Ca_e = 0.40$, maintaining the same numerical parameters as in the previous cases (Sec. IV C 2). Here, the domain size is $L_x \times L_y \times L_z = 30R_0 \times 8R_0 \times 4R_0$, and a wide range of viscosity ratio ($0.01 \leq \lambda \leq 10$) was considered.

Breakage of the surfactant-laden drop was observed at $Ca_e = 0.40$ for $0.05 \leq \lambda \leq 1.7$. The breakage progress in $\lambda = 1.05$ and the

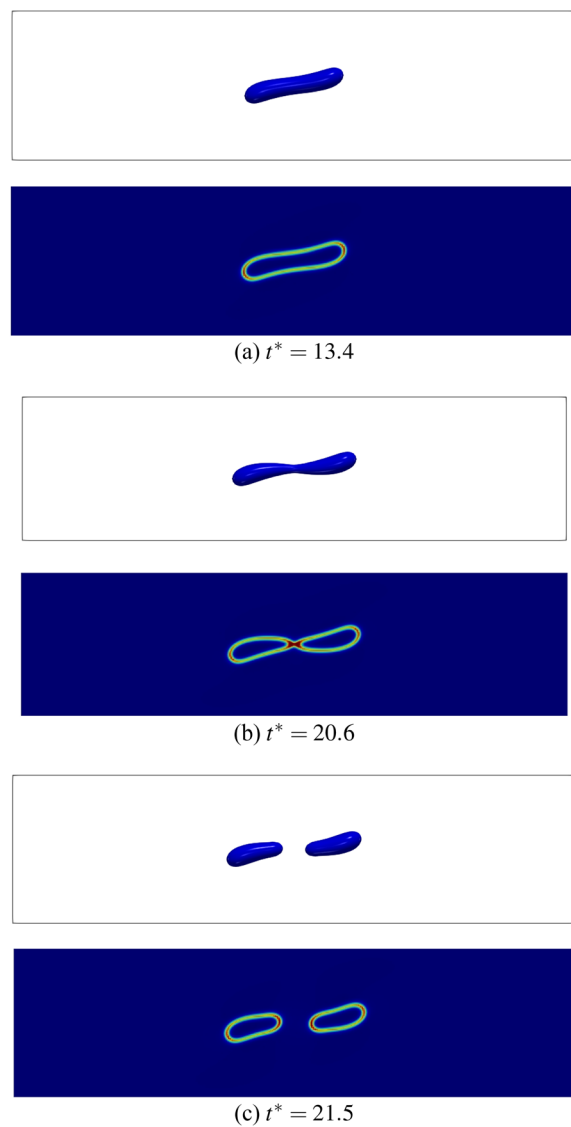


FIG. 16. The snapshots at different time scales for $\lambda = 1.05$; $Re = 0.0625$; $Ca_e = 0.40$, $\psi_b = 0.1$. Top: drop morphology; Bottom: surfactant concentration in the domain.

evaluation of ψ field are shown in Fig. 16. The surfactant accumulates at the drop tips and the thin neck during deformation, promoting localized deformation.

Comparative visuals of drop shapes and internal circulations, specifically for $\lambda = 0.05$ and $\lambda = 1.7$ right before drop breaks, are displayed in Fig. 17. For $\lambda = 0.05$, the drop, with a higher viscosity than that of its surrounding fluid, predominantly elongates along the shear direction. Conversely, for $\lambda = 1.7$, the surrounding high viscosity fluid hinders the drop deformation.

As the viscosity ratio between phases increases, the surfactant-laden drop does not break. The effect of viscosity becomes dominant such that even with the presence of surfactant, the drop reaches the

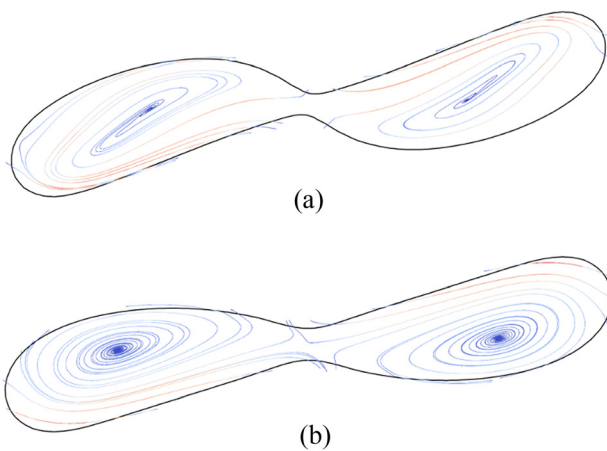


FIG. 17. The drop shape and its internal circulations for $\psi_b = 0.1$, $Re = 0.0625$, $Ca_e = 0.40$ just before breakage: (a) $\lambda = 0.05$ and (b) $\lambda = 1.7$.

equilibrium shape. Figure 18 shows the final drop shape and its internal recirculations for λ ranging from 0.01 to 10. For $\lambda < 1$, dual recirculations are evident, whereas for $\lambda > 1$, a single recirculation is observed. The drop deforms and rotates less with increasing viscosity ratio when $\lambda < 0.05$; the drop deforms less but rotates more with increasing λ when $\lambda > 1.7$.

In summary, the presence of surfactant overcomes the effect of viscosity ratio for a system with moderate viscosity ratio ($0.05 \leq \lambda \leq 1.7$), leading to drop breakage and lowering the critical capillary number. More specifically, drop breakage was observed at $\lambda = 0.05, 0.1, 0.2, 0.3, 0.4, 0.5, 0.6, 0.7, 0.8, 0.9, 1.05, 1.1, 1.2, 1.3, 1.4, 1.5, 1.6, 1.7$ for $Ca_e = 0.40$ and $Re = 0.0625$. The surfactant fails to cause breakage when drops are highly viscous (either $\lambda <$

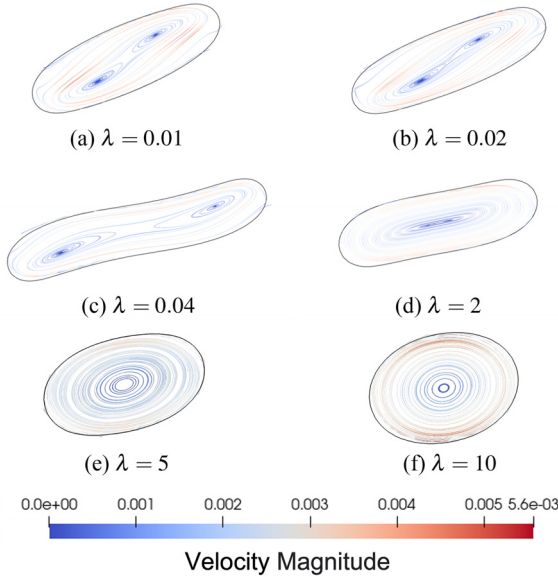


FIG. 18. The snapshots of the drop morphology at equilibrium for different λ with $\psi_b = 0.1$ and $Ca_e = 0.4$: the black curve represents the interface, and the internal re-circulations are colored with velocity magnitude.

0.05 or $\lambda > 1.7$). Drops with $\lambda = 0.01, 0.02, 0.04, 1.8, 2, 5, 10$ remain stable.

4. Effect of surfactant concentration

This section focuses on understanding how the surfactant concentration influences drop deformation. According to the EOS [Eq. (16)], the higher the bulk surfactant concentration is, the more surfactant absorbs at the surface. High surfactant load leads to higher decrease in surface tension. We hence perform simulations with bulk surfactant concentration $\psi_b = \{0.5 \times 10^{-2}, 1 \times 10^{-1}, 2 \times 10^{-1}\}$ with $Re = 0.0625$ at $Ca = 0.05, 0.12$ and $Ca = 0.2$, with $\lambda = 1$. Other numerical parameters are kept the same as in Sec. IV C2.

A comparative analysis of drop shape for different surfactant loads at equilibrium is presented in Fig. 19. Here, black, red, and blue curves represent the cases at $\psi_b = 0.05, 0.1$, and 0.2 , respectively. The capillary number is $0.05, 0.12$, and 0.2 from left to right.

Under the same capillary number, a higher bulk surfactant concentration amplifies drop deformation. Additionally, the deviation of drop deformation with different surfactant loads

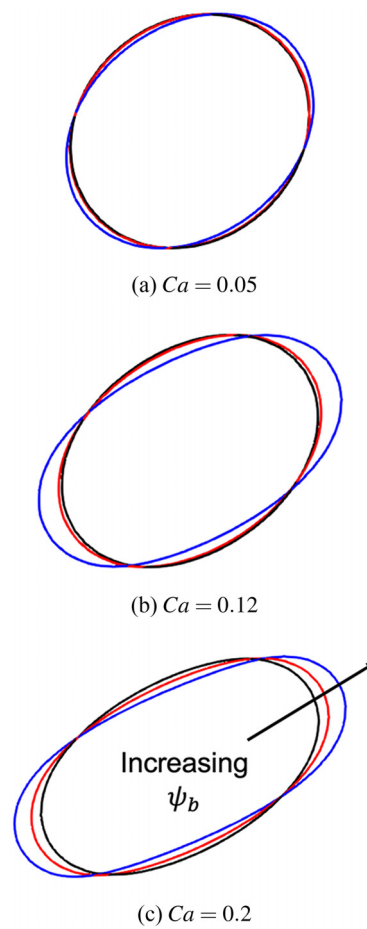


FIG. 19. The snapshots of the drop morphology at equilibrium with different surfactant loads: $\psi_b = 0.05$ (black), $\psi_b = 0.1$ (red), and $\psi_b = 0.2$ (blue).

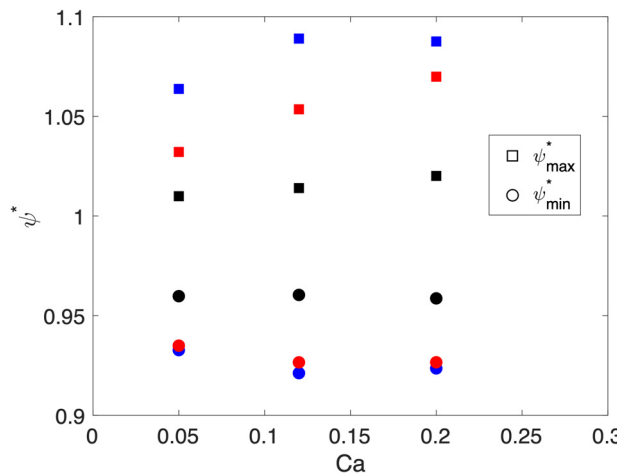


FIG. 20. Dimensionless surfactant concentration as a function of the capillary number: square markers represent the maximum and the star markers represent the minimum ψ^* ; the blue, red, and black markers stand for $\psi_b = 0.05, 0.1$, and 0.2 , respectively.

increases as Ca increases. To better understand this trend, the maximum and minimum values of the dimensionless surfactant concentration ψ^* at the interface are plotted as a function of Ca in Fig. 20. For a given Ca , the non-uniformity of the surfactant at the interface increases with the increase in surfactant load. The drop is more likely to elongate. As Ca increases, we observe a decrease in the maximum ψ^* for $\psi_b = 0.2$ at $Ca = 0.2$. This is because the current effective capillary number Ca_e for $\psi_b = 0.2$ is in regime III as explained in Sec. IV C 2. Herein, the Marangoni and surface dilution effects influence the surfactant distribution. Despite this, the peak ψ^* value at the interface exceeds those observed for the other surfactant loads, and hence, the drop deformation at $\psi_b = 0.2$ is still larger than when $\psi_b = 0.1$ or 0.05 .

The higher surfactant load also leads to earlier drop breakage during shearing, as shown in Fig. 21: when $Ca = 0.25$, surfactant-laden drop with $\psi_b = 0.2$ breaks while those with $\psi_b = 0.1$ and 0.05 remains stable. The corresponding Ca_e are also given: Ca_e for drop with $\psi_b = 0.2$ is above the critical capillary number for pure drops ($Ca = 0.41$), leading to breakage, whereas Ca_e for drop with $\psi_b = 0.1$ and 0.05 is 0.35 and 0.31 , respectively, keeping the drop stable.

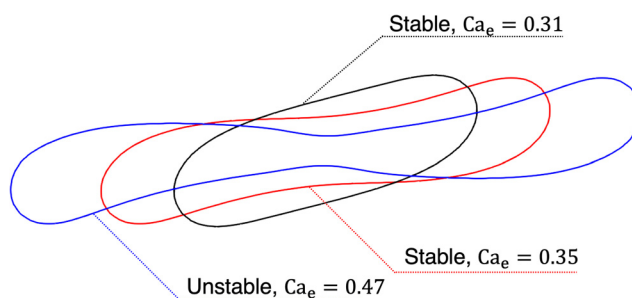


FIG. 21. The drop shapes at $Ca = 0.25$: black curves represent $\psi_b = 0.05$; red curves represent $\psi_b = 0.12$; blue curves represent $\psi_b = 0.2$.

V. CONCLUSIONS

In this study, we introduced, verified, and validated a diffuse interface lattice Boltzmann method to simulate a system of immiscible liquids with nonionic soluble surfactants. This method couples the Navier–Stokes equations with a conservative Allen–Cahn phase field equation and a Cahn–Hilliard surfactant transport equation. The terms of these transport equations were deduced based on a modified Ginzburg–Landau functional free energy functional. We validate the method using the interfacial profile of the planar interface and equilibrating drops against their analytical solutions. Our method can accurately capture the interface and surfactant behaviors with varying bulk surfactant loads for both Langmuir and Frumkin isotherms. Terms involving ψ in chemical potential are kept while eliminating unwanted interfacial behaviors (surface broadening or location shifting). Additionally, the method accommodates different surfactant solubilities in bulk phases. The surface tension decrease in drop equilibration is well aligned with EOS. A noteworthy feature of our method is its diminutive spurious velocities, which are approximately 10^{-6} .

We further conducted simulations of surfactant-laden drop dynamics in a simple shear flow. A series of benchmarks meticulously identified the values of two numerical dimensionless numbers that capture the drop behavior at given physical dimensionless numbers ($Pe = 0.0826$ and $Ch = 0.15$). We subsequently investigated the effects of the capillary number, interplay of surfactant and viscosity ratio, and surfactant concentration on drop deformation. The numerical results show that at a given Ca , surfactant-laden drops develop a non-uniform ψ distribution at the interface and, thus, deform more than pure drops. The non-uniform surfactant distribution leads to three additional effects: tip-stretching, Marangoni, and surface dilution. These effects either amplify the non-uniformity of ψ (as in tip-stretching) or hinder it (as seen with Marangoni and surface dilution effects). The non-uniformity of ψ at the interface as a function of Ca is categorized into three regimes based on the competing influence of these effects. As Ca continues to increase, the drop undergoes a breakage. The presence of surfactant and viscosity ratio have a competing effect against each other since the former promotes drop breakage, and the latter hinders it. The presence of surfactant can overcome the effect of viscosity ratio (with a viscosity ratio $0.05 \leq \lambda \leq 1.7$) and lowers the critical capillary number, promoting drop breakup. Highly viscous drops do not break due to the strong effect of the viscosity ratio, even when surfactant is present. Surfactant-laden drop breakage can also be achieved by the presence of a high load of surfactant, whereby drop breaks even at a low Ca value.

Our method offers a promising potential in describing emulsions with nonionic soluble surfactants. Through this study, we present comprehensive three-dimensional results and accommodate generic general surfactant isotherms. We detailedly captured and analyzed critical physical phenomena brought by the presence of surfactant. From a numerical perspective, our approach has high accuracy and low artifact. Therefore, our method can benefit and pave the way for advancements in the emulsion production industry.

ACKNOWLEDGMENTS

The financial support provided by the Natural Sciences and Engineering Research Council of Canada (NSERC) Discovery Grant is gratefully acknowledged. This research was enabled in part by

support provided by the Digital Research Alliance of Canada (<https://alliancecan.ca/en>). We gratefully acknowledge the support from Canada First Research Excellence Fund (CFREF) and Future Energy System (FES) T02P05 at the University of Alberta. P.A.T. holds a Canada Research Chair (CRC) in Fluids and Interfaces (No. CRC 233147) and gratefully acknowledges funding from the Alberta Innovates (AI) and NSERC Discovery Grant (No. RGPIN-2020-05511).

AUTHOR DECLARATIONS

Conflict of Interest

The authors have no conflicts to disclose.

Author Contributions

Zhe (Ashley) Chen: Conceptualization (equal); Data curation (equal); Formal analysis (equal); Investigation (equal); Methodology (equal);

Software (equal); Validation (equal); Visualization (equal); Writing – original draft (equal). **Peichun Amy Tsai:** Conceptualization (equal); Funding acquisition (equal); Resources (equal); Supervision (equal); Visualization (equal); Writing – review & editing (equal). **Alexandra Komrakova:** Conceptualization (equal); Funding acquisition (equal); Supervision (equal); Visualization (equal); Writing – review & editing (equal).

DATA AVAILABILITY

The data that support the findings of this study are available from the corresponding author upon reasonable request.

APPENDIX A: LATTICE STRUCTURE

The discrete velocity set for D3Q27 model is defined as

$$e_{\alpha}^f \begin{pmatrix} 0 & 1 & -1 & 0 & 0 & 0 & 0 & 1 & -1 & 1 & -1 & 1 & -1 & 1 & -1 & 1 & -1 & 1 & -1 & 1 & -1 & 1 & -1 & 1 & -1 & 1 & -1 & 1 & -1 & 0 & 0 & 0 & 0 \\ 0 & 0 & 0 & 1 & -1 & 0 & 0 & 1 & 1 & -1 & -1 & 1 & 1 & -1 & -1 & -1 & 1 & 1 & -1 & -1 & 1 & 1 & -1 & -1 & 0 & 0 & 0 & 1 & -1 & 1 & -1 & -1 \\ 0 & 0 & 0 & 0 & 0 & 1 & -1 & 1 & 1 & 1 & 1 & -1 & 1 & -1 & -1 & -1 & 0 & 0 & 0 & 0 & 1 & 1 & -1 & 1 & 1 & -1 & -1 & -1 & -1 \end{pmatrix}.$$

The corresponding weights are

$$\omega_{\alpha}^f = \begin{cases} \frac{64}{216}, & \alpha = 0, \\ \frac{16}{216}, & \alpha = 1 - 6, \\ \frac{1}{216}, & \alpha = 7 - 14, \\ \frac{4}{216}, & \alpha = 15 - 26. \end{cases} \quad (\text{A1})$$

The discrete velocity set for D3Q15 model is defined as

$$e_{\alpha}^g \begin{pmatrix} 0 & 1 & -1 & 0 & 0 & 0 & 0 & 1 & -1 & 1 & -1 & 1 & -1 & 1 & -1 & 1 & -1 \\ 0 & 0 & 0 & 1 & -1 & 0 & 0 & 1 & 1 & -1 & -1 & 1 & 1 & -1 & -1 & 1 & -1 & -1 \\ 0 & 0 & 0 & 0 & 0 & 1 & -1 & 1 & 1 & 1 & 1 & -1 & -1 & -1 & -1 & -1 & -1 & -1 \end{pmatrix}$$

with the corresponding weights

$$\omega_{\alpha}^g = \begin{cases} \frac{16}{72}, & \alpha = 0, \\ \frac{8}{72}, & \alpha = 1 - 6, \\ \frac{1}{72}, & \alpha = 7 - 14. \end{cases} \quad (\text{A2})$$

APPENDIX B: WMRT TRANSFORMATION MATRIX

The orthogonal transformation matrix \mathbf{M} is adapted from the weighted-multiple-relaxation-time (WMRT) scheme, proposed by Fakhari *et al.*³⁸

$$M = \begin{pmatrix} 1 & 1 \\ 0 & 1 & -1 & 0 & 0 & 0 & 0 & 1 & -1 & 1 & -1 & 1 & -1 & 1 & -1 & 1 & -1 & 1 & -1 & 1 & -1 & 1 & -1 & 1 & -1 & 0 & 0 & 0 & 0 & 0 \\ 0 & 0 & 0 & 1 & -1 & 0 & 0 & 1 & 1 & -1 & -1 & 1 & 1 & -1 & -1 & 1 & 1 & -1 & -1 & 0 & 0 & 0 & 0 & 1 & 1 & -1 & -1 & 1 & 1 & -1 & -1 \\ 0 & 0 & 0 & 0 & 0 & 1 & -1 & 1 & 1 & 1 & 1 & -1 & -1 & -1 & -1 & 0 & 0 & 0 & 0 & 1 & 1 & -1 & -1 & 1 & 1 & 1 & -1 & -1 & -1 \\ 0 & 0 & 0 & 0 & 0 & 0 & 0 & 1 & -1 & -1 & 1 & 1 & -1 & -1 & -1 & 1 & 1 & -1 & -1 & 1 & 0 & 0 & 0 & 0 & 0 & 0 & 0 & 0 & 0 & 0 & 0 \\ 0 & 0 & 0 & 0 & 0 & 0 & 0 & 1 & 1 & -1 & -1 & -1 & -1 & -1 & -1 & 1 & 1 & -1 & -1 & 1 & 0 & 0 & 0 & 0 & 0 & 0 & 0 & 0 & 0 & 0 & 0 \\ 0 & 0 & 0 & 0 & 0 & 0 & 0 & 1 & 1 & -1 & -1 & -1 & -1 & -1 & -1 & 1 & 1 & -1 & -1 & 1 & 0 & 0 & 0 & 0 & 0 & 0 & 0 & 0 & 1 & -1 & -1 \\ 0 & 0 & 0 & 0 & 0 & 0 & 0 & 1 & 1 & -1 & -1 & -1 & -1 & -1 & -1 & 1 & 1 & -1 & -1 & 1 & 0 & 0 & 0 & 0 & 0 & 0 & 0 & 0 & 1 & -1 & -1 \\ 0 & 0 & 0 & 0 & 0 & 0 & 0 & 1 & -1 & 1 & -1 & -1 & -1 & -1 & -1 & 1 & 0 & 0 & 0 & 0 & 1 & -1 & -1 & 1 & 0 & 0 & 0 & 0 & 0 & 0 \\ 0 & 0 & 0 & 0 & 0 & 0 & 0 & 1 & -1 & 1 & -1 & -1 & -1 & -1 & -1 & 1 & 1 & 1 & 1 & 1 & 1 & 1 & 1 & 1 & -2 & -2 & -2 & -2 \\ 0 & 0 & 0 & 1 & 1 & -1 & -1 & 0 & 0 & 0 & 0 & 0 & 0 & 0 & 0 & 1 & 1 & 1 & 1 & 1 & -1 & -1 & -1 & -1 & 0 & 0 & 0 & 0 & 0 & 0 \\ -1 & 0 & 0 & 0 & 0 & 0 & 2 & 2 & 2 & 2 & 2 & 2 & 2 & 2 & 2 & 1 & 1 & 1 & 1 & 1 & 1 & 1 & 1 & 1 & 1 & 1 & 1 & 1 & 1 & 1 & 1 \\ 0 & -2 & 2 & 0 & 0 & 0 & 0 & 4 & -4 & 4 & -4 & 4 & -4 & 4 & -4 & 1 & -1 & 1 & -1 & 1 & -1 & 1 & -1 & 1 & 0 & 0 & 0 & 0 & 0 & 0 & 0 \\ 0 & 0 & 0 & -2 & 2 & 0 & 0 & 4 & 4 & -4 & -4 & 4 & 4 & -4 & -4 & 1 & 1 & -1 & -1 & 0 & 0 & 0 & 0 & 1 & 1 & -1 & -1 & 1 & 1 & -1 \\ 0 & 0 & 0 & 0 & 0 & -2 & 2 & 4 & 4 & 4 & 4 & -4 & -4 & -4 & -4 & 0 & 0 & 0 & 0 & 1 & 1 & -1 & -1 & 1 & 1 & 1 & -1 & -1 & -1 \\ 0 & 0 & 0 & 0 & 0 & 0 & 0 & 0 & 0 & 0 & 0 & 0 & 0 & 0 & 0 & 0 & 1 & -1 & 1 & -1 & -1 & 1 & 1 & -1 & 1 & 0 & 0 & 0 & 0 & 0 & 0 \\ 0 & 0 & 0 & 0 & 0 & 0 & 0 & 0 & 0 & 0 & 0 & 0 & 0 & 0 & 0 & 0 & -1 & -1 & 1 & 1 & 0 & 0 & 0 & 0 & 1 & -1 & 1 & -1 & -1 \\ 0 & 0 \\ 0 & 0 & 0 & 0 & 0 & 0 & 0 & 0 & 1 & -1 & -1 & 1 & -1 & 1 & 1 & -1 & 0 & 0 & 0 & 0 & 0 & 0 & 0 & 0 & 0 & 0 & 0 & 0 & 0 & 0 & 0 \\ 1 & -1 & -1 & -1 & -1 & -1 & -1 & -1 & 4 & 4 & 4 & 4 & 4 & 4 & 4 & 4 & 0 & 0 & 0 & 0 & 0 & 0 & 0 & 0 & 0 & 0 & 0 & 0 & 0 & 0 & 0 \\ 0 & -2 & -2 & 1 & 1 & 1 & 1 & 0 & 0 & 0 & 0 & 0 & 0 & 0 & 0 & 0 & 2 & 2 & 2 & 2 & 2 & 2 & 2 & 2 & 2 & -4 & -4 & -4 & -4 & -4 & -4 \\ 0 & 0 & 0 & -1 & -1 & 1 & 1 & 0 & 0 & 0 & 0 & 0 & 0 & 0 & 0 & 0 & 2 & 2 & 2 & 2 & 2 & 2 & 2 & 2 & 2 & -2 & -2 & -2 & -2 & 0 & 0 & 0 & 0 \\ 0 & 0 & 0 & 0 & 0 & 0 & 0 & 0 & 2 & -2 & -2 & 2 & 2 & -2 & -2 & 2 & -1 & 1 & 1 & -1 & 0 & 0 & 0 & 0 & 0 & 0 & 0 & 0 & 0 & 0 & 0 \\ 0 & 0 & 0 & 0 & 0 & 0 & 0 & 0 & 2 & 2 & -2 & -2 & -2 & -2 & -2 & 2 & 0 & 0 & 0 & 0 & 0 & 0 & 0 & 0 & 0 & 0 & 0 & 0 & 0 & 0 & 0 \\ 0 & 0 & 0 & 0 & 0 & 0 & 0 & 0 & 2 & -2 & 2 & -2 & -2 & -2 & 2 & -2 & 0 & 0 & 0 & 0 & -1 & 1 & 1 & -1 & 0 & 0 & 0 & 0 & 0 & 0 & 0 \\ 0 & 0 & 1 & -1 & 0 & 0 & 0 & 0 & 4 & -4 & 4 & -4 & 4 & -4 & 4 & -4 & -2 & 2 & -2 & 2 & -2 & 2 & -2 & 2 & 0 & 0 & 0 & -2 & 2 & -2 & 2 \\ 0 & 0 & 0 & 1 & -1 & 0 & 0 & 0 & 4 & 4 & -4 & -4 & 4 & -4 & 4 & -4 & -2 & -2 & -2 & 2 & 2 & 2 & 0 & 0 & 0 & 0 & -2 & 2 & -2 & 2 & 2 \\ 0 & 0 & 0 & 0 & 0 & 1 & -1 & 4 & 4 & 4 & 4 & -4 & -4 & -4 & -4 & 0 & 0 & 0 & 0 & 0 & -2 & -2 & 2 & 2 & -2 & -2 & 2 & 2 & 2 \\ -1 & 2 & 2 & 2 & 2 & 2 & 2 & 2 & -8 & 8 & 8 & 8 & 8 & 8 & 8 & 8 & 8 & 8 & 8 & -4 & -4 & -4 & -4 & -4 & -4 & -4 & -4 & -4 & -4 & -4 \end{pmatrix} .$$

APPENDIX C: DETAILED LATTICE BOLTZMANN CALCULATION

1. Particle distribution f_x

The modified equilibrium distribution function, \bar{f}_x^{eq} , in Eq. (17a) is calculated by subtracting half of the forcing term from the regular equilibrium distribution function to simplify the collision step²⁴ as

$$\bar{f}_x^{eq} = f_x^{eq} - \frac{1}{2} F_x \quad (C1)$$

with

$$f_x^{eq} = \omega_x \left[p^* + \left(\frac{\mathbf{e}_x \cdot \mathbf{u}}{c_s^2} + \frac{(\mathbf{e}_x \cdot \mathbf{u})^2}{2c_s^4} - \frac{\mathbf{u} \cdot \mathbf{u}}{2c_s^2} \right) \right]. \quad (C2)$$

In Eq. (17a), the diagonal relaxation matrix is

$$\hat{\mathbf{S}} = (1, 1, 1, 1, s_\nu, s_\nu, s_\nu, s_\nu, s_\nu, 1, \dots, 1). \quad (C3)$$

The relaxation parameter (s_ν) relates to the hydrodynamic time (τ_f) as

$$s_\nu = 1/(\tau_f + 0.5). \quad (C4)$$

The viscosity is set as

$$\mu = \rho\nu = \rho\tau_f c_s^2, \quad (C5)$$

where ν is the bulk kinematic viscosity and μ and ρ are the bulk dynamic viscosity and density, respectively. The relaxation time τ_f is calculated by

$$\tau_f = \tau_L + \phi(\tau_H - \tau_L), \quad (C6)$$

where τ_L and τ_H are the bulk relaxation times for the light and heavy fluids, respectively.

The hydrodynamics forcing term $F_x(\mathbf{x}, t)$ in Eq. (17a) is given by

$$F_x(\mathbf{x}, t) = \omega_x \frac{\mathbf{e}_x \cdot \mathbf{F}_s}{\rho c_s^2}. \quad (C7)$$

The way that the modified equilibrium distribution function was shifted by half of the forcing term is especially crucial for the velocity-related functions (f_x) to increase the model stability.

2. Particle distribution g_x

The equilibrium distribution term \bar{g}_x^{eq} is calculated as a result of a shift from the forcing term

$$\bar{g}_x^{eq}(\mathbf{x}, t) = g_x^{eq} - \frac{1}{2} F_x^\phi, \quad (C8)$$

where

$$g_x^{eq} = \phi \omega_x \left(1 + \frac{\mathbf{e}_x \cdot \mathbf{u}}{c_s^2} + \frac{(\mathbf{e}_x \cdot \mathbf{u})^2}{2c_s^4} - \frac{\mathbf{u} \cdot \mathbf{u}}{2c_s^2} \right). \quad (C9)$$

The phase-field relaxation time in Eq. (17b) is defined as $\tau_\phi = M_\phi / (c_s^2 \delta t)$. The forcing term F_α^ϕ in Eq. (17b) is defined as²⁷

$$F_\alpha^\phi(\mathbf{x}, t) = \delta t \frac{4\phi(1-\phi)}{\zeta} \omega_\alpha \mathbf{e}_\alpha \cdot \hat{\mathbf{n}}. \quad (\text{C10})$$

3. Particle distribution h_α

The equilibrium distribution term h_α^{eq} (from $\alpha=1$ to $\alpha=14$) is calculated as

$$h_\alpha^{eq} = \omega_\alpha \left(\frac{\Gamma_\psi \mu_\psi}{c_s^2} + \psi \frac{\mathbf{e}_\alpha \cdot \mathbf{u}}{c_s^2} + \psi \frac{(\mathbf{e}_\alpha \cdot \mathbf{u})^2}{2c_s^4} - \psi \frac{\mathbf{u} \cdot \mathbf{u}}{2c_s^2} \right). \quad (\text{C11})$$

The populations for $q=0$ are calculated separately by

$$h_0^{eq} = \psi - \sum_{i=1}^{14} h_i^{eq}. \quad (\text{C12})$$

4. Gradients and Laplacian calculation

To minimize the numerical error, the gradients and Laplacian of the order parameter variables in our method are determined using a second-order, isotropic centered difference scheme and then executed the dot product according to previous studies^{32,56}

$$\nabla \phi \approx \frac{c}{c_s^2 \delta x} \sum_{\alpha=0}^{26} \mathbf{e}_\alpha \omega_\alpha \phi(\mathbf{x} + \mathbf{e}_\alpha \delta t, t), \quad (\text{C13})$$

$$\nabla^2 \phi \approx \frac{2c^2}{c_s^2 (\delta x)^2} \sum_{i=0}^{26} \omega_\alpha [\phi(\mathbf{x} + \mathbf{e}_\alpha \delta t, t) - \phi(\mathbf{x}, t)]. \quad (\text{C14})$$

For the D3Q27 model, the implementation for Eq. (C17) can be calculated as⁵⁷

$$\nabla^2 \phi \approx \frac{1}{36} \left[16 \sum_{i=1}^6 \phi_i^{(1)} + 4 \sum_{i=1}^{12} \phi_i^{(2)} + \sum_{i=1}^8 \phi_i^{(3)} - 152 \phi^{(0)} \right], \quad (\text{C15})$$

where $\phi_i^{(1)}$, $\phi_i^{(2)}$, and $\phi_i^{(3)}$ stand for the nearest, second-nearest, and third-nearest points nearby, respectively.

Similarly, the gradients and Laplacian of the surfactant-field variable will be

$$\nabla \psi \approx \frac{c}{c_s^2 \delta x} \sum_{\alpha=0}^{14} \mathbf{e}_\alpha \omega_\alpha \psi(\mathbf{x} + \mathbf{e}_\alpha \delta t, t), \quad (\text{C16})$$

$$\nabla^2 \psi \approx \frac{2c^2}{c_s^2 (\delta x)^2} \sum_{i=0}^{14} \omega_\alpha [\psi(\mathbf{x} + \mathbf{e}_\alpha \delta t, t) - \psi(\mathbf{x}, t)]. \quad (\text{C17})$$

APPENDIX D: BENCHMARK FOR PECLET AND CAHN NUMBERS ON NUMERICAL RESULTS

The following physical parameters are specified: $Re = 0.0625$, $Ca = 0.45$, and $\lambda = 1$. The influence of Pe and Ch on the result for a fixed drop radius of $a = 20$ lattice units is shown in Table I.

The data in the table are organized in the following way: the Pelet number decreases from left to right, while the Cahn number increases from top to bottom. An increase in the Pe number and the

TABLE I. Drop shape for drop with radius $R_0 = 30$ at $Re = 0.0625$, $Ca = 0.45$, and $\lambda = 1$ at different Pe and Ch numbers.

	Pe = 0.082 26	Pe = 0.016 452	Pe = 0.008 26
Ch = 0.1			Not stable
Ch = 0.15			Not stable
Ca = 0.2			Not stable

Ch number results in increased drop deformation for every case: the drop becomes more elongated and is easier to break. According to the reference data in Ref. 46, drop breaks when $Ca = 0.45$. The proper choice for set of number parameters can be selected to match the literature data.

APPENDIX E: ADDITIONAL BENCHMARK FOR SHEARING IN A SURFACTANT-FREE SYSTEM

A set of good choice of numerical parameters are needed for this dynamic system in order to provide physical results. In this section, we provide benchmarks for surfactant-free drop in shear flow. Two benchmarks are first chosen from the previous research from the previous research:^{46,58} (1) $Re = 0.0625$, $Ca = 0.1$, and $\lambda = 1$; (2) $Re = 1$, $Ca = 0.27$, and $\lambda = 1$. The choice of the numerical parameters was set as follows: $\xi = 3$, $\sigma_0 = 0.01$, $\tau_g = 1$, and $M_\phi = 0.15$. The steady state drop shape and the corresponding streamlines are shown in Fig. 22. The reference data for case (1) are from Li *et al.*⁴⁶ with $D_T = 0.119$, and our simulation result is $D_T = 0.114$, showing a 4.2% deviation. The reference data for case (2) are from Renardy and Cristini⁵⁸ with $L/R_0 = 1.8$. Our simulation result is $L/R_0 = 1.74$, showing a 3.3% deviation. These results are shown in Fig. 22, and they match well for a dynamic system.

It is worth mentioning that in order to satisfy the specific conditions in the above validation cases, we chose to alter the relaxation time τ (correspondingly, the absolute value of fluid viscosity μ), while keeping the interfacial tension σ the same. The interfacial tension will be decreased after the introduction of the surfactant (as shown in Fig. 4), and choosing a small σ in absolute value might make the decrease itself unnoticeable. The cases above shows a promising range for τ , giving us the flexibility to test for various conditions in the following sections.



FIG. 22. Steady state drop shape: (a) $Re = 0.0625$, $Ca = 0.1$, $\lambda = 1$; (b) $Re = 1$, $Ca = 0.27$, $\lambda = 1$. Red part represents the drop, black curve represents the interface, and white lines are the internal velocity streamlines.

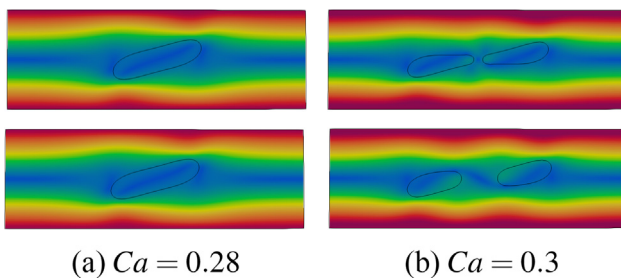


FIG. 23. Drop's detailed deformation process at the same moment for $\lambda = 2$: the left two pictures are for $Ca = 0.28$, and the right two pictures are for $Ca = 0.3$. The black curvature represents for the drop shape, and the velocity field is added on top of the plots.

APPENDIX F: ADDITIONAL BENCHMARK FOR SHEARING IN A SURFACTANT-FREE SYSTEM WITH VISCOSITY RATIO

The ability of our model to accurately capture a system with a viscosity ratio has been validated in our previously published papers.^{25,54} In addition, we performed two cases with (a) $\lambda = 2$, $Re = 1$, and $Ca = 0.28$ and (b) $\lambda = 2$, $Re = 1$, and $Ca = 0.3$. These two cases were performed in a slightly confined channel, and the simulation domain is set as $L_x \times L_y \times L_z = 12a \times 4a \times 4a$. According to Komrakova *et al.*,⁴⁷ case (a) will maintain a steady shape, while case (b) will have a drop breakage. The deformation process is compared in Fig. 23, and the deformation patterns are consistent with the results from Ref. 47.

REFERENCES

- ¹A. Nesterenko, A. Drelich, H. Lu, D. Clausse, and I. Pezron, "Influence of a mixed particle/surfactant emulsifier system on water-in-oil emulsion stability," *Colloids Surf. A* **457**, 49–57 (2014).
- ²M. Zembyla, B. S. Murray, and A. Sarkar, "Water-in-oil emulsions stabilized by surfactants, biopolymers and/or particles: A review," *Trends Food Sci. Technol.* **104**, 49–59 (2020).
- ³H. Liu and Y. Zhang, "Phase-field modeling droplet dynamics with soluble surfactants," *J. Comput. Phys.* **229**, 9166–9187 (2010).
- ⁴A. K. Pennathur, C. Tseng, N. Salazar, and J. M. Dawlaty, "Controlling water delivery to an electrochemical interface with surfactants," *J. Am. Chem. Soc.* **145**, 2421–2429 (2023).
- ⁵D. Langevin and F. Monroy, "Marangoni stresses and surface compression rheology of surfactant solutions. Achievements and problems," *Adv. Colloid Interface Sci.* **206**, 141–149 (2014).
- ⁶G. Soligo, A. Roccon, and A. Soldati, "Coalescence of surfactant-laden drops by phase field method," *J. Comput. Phys.* **376**, 1292–1311 (2019).
- ⁷Y. Zong, C. Zhang, H. Liang, L. Wang, and J. Xu, "Modeling surfactant-laden droplet dynamics by lattice Boltzmann method," *Phys. Fluids* **32**, 122105 (2020).
- ⁸Y. Sun and C. Beckermann, "Sharp interface tracking using the phase-field equation," *J. Comput. Phys.* **220**, 626–653 (2007).
- ⁹S. Mirjalili, S. S. Jain, and M. Dodd, "Interface-capturing methods for two-phase flows: An overview and recent developments," *Center for Turbulence Research Annual Research Briefs* (Center for Turbulence Research, 2017), pp. 117–135.
- ¹⁰R. Qin and H. Bhadeshia, "Phase field method," *Mater. Sci. Technol.* **26**, 803–811 (2010).
- ¹¹A. J. James and J. Lowengrub, "A surfactant-conserving volume-of-fluid method for interfacial flows with insoluble surfactant," *J. Comput. Phys.* **201**, 685–722 (2004).
- ¹²M. Muradoglu and G. Tryggvason, "A front-tracking method for computation of interfacial flows with soluble surfactants," *J. Comput. Phys.* **227**, 2238–2262 (2008).
- ¹³X. Shang, Z. Luo, B. Bai, and G. Hu, "A front-tracking method for simulating interfacial flows with particles and soluble surfactants," *J. Comput. Phys.* **493**, 112476 (2023).
- ¹⁴J.-J. Xu, Y. Yang, and J. Lowengrub, "A level-set continuum method for two-phase flows with insoluble surfactant," *J. Comput. Phys.* **231**, 5897–5909 (2012).
- ¹⁵Y. Shi, G. Tang, L. Cheng, and H. Shuang, "An improved phase-field-based lattice Boltzmann model for droplet dynamics with soluble surfactant," *Comput. Fluids* **179**, 508–520 (2019).
- ¹⁶W. Zhou, Y. Xing, X. Liu, and Y. Yan, "Modeling of droplet dynamics with soluble surfactant by multi-relaxation-time phase-field lattice Boltzmann method," *Phys. Fluids* **35**, 012109 (2023).
- ¹⁷J. Farhadi and V. Bazargan, "Marangoni flow and surfactant transport in evaporating sessile droplets: A lattice Boltzmann study," *Phys. Fluids* **34**, 032115 (2022).
- ¹⁸E. Kian Far, M. Gorakifard, and M. Goraki Fard, "A new three dimensional cumulant phase field lattice Boltzmann method to study soluble surfactant," *Phys. Fluids* **35**, 053338 (2023).
- ¹⁹R. Van der Sman and S. Van der Graaf, "Diffuse interface model of surfactant adsorption onto flat and droplet interfaces," *Rheol. Acta* **46**, 3–11 (2006).
- ²⁰R. G. van der Sman and M. Meinders, "Analysis of improved lattice Boltzmann phase field method for soluble surfactants," *Comput. Phys. Commun.* **199**, 12–21 (2016).
- ²¹A. Yun, Y. Li, and J. Kim, "A new phase-field model for a water–oil–surfactant system," *Appl. Math. Comput.* **229**, 422–432 (2014).
- ²²P.-H. Chiu and Y.-T. Lin, "A conservative phase field method for solving incompressible two-phase flows," *J. Comput. Phys.* **230**, 185–204 (2011).
- ²³V. Badalassi, H. Ceniceros, and S. Banerjee, "Computation of multiphase systems with phase field models," *J. Comput. Phys.* **190**, 371–397 (2003).
- ²⁴A. Fakhari, T. Mitchell, C. Leonardi, and D. Bolster, "Improved locality of the phase-field lattice-Boltzmann model for immiscible fluids at high density ratios," *Phys. Rev. E* **96**, 053301 (2017).
- ²⁵Z. A. Chen, F. Huang, P. A. Tsai, and A. Komrakova, "Numerical study of microfluidic emulsion dynamics under the influence of heterogeneous surface wettability," *Int. J. Multiphase Flow* **147**, 103863 (2022).
- ²⁶D. Jacqmin, "Calculation of two-phase Navier–Stokes flows using phase-field modeling," *J. Comput. Phys.* **155**, 96–127 (1999).
- ²⁷T. Mitchell, C. Leonardi, and A. Fakhari, "Development of a three-dimensional phase-field lattice Boltzmann method for the study of immiscible fluids at high density ratios," *Int. J. Multiphase Flow* **107**, 1–15 (2018).
- ²⁸G. Soligo, A. Roccon, and A. Soldati, "Breakage, coalescence and size distribution of surfactant-laden droplets in turbulent flow," *J. Fluid Mech.* **881**, 244–282 (2019).
- ²⁹G. Zhu, J. Kou, B. Yao, Y. Wu, J. Yao, and S. Sun, "Thermodynamically consistent modelling of two-phase flows with moving contact line and soluble surfactants," *J. Fluid Mech.* **879**, 327–359 (2019).

- ³⁰S. Engblom, M. Do-Quang, G. Amberg, and A.-K. Tornberg, "On diffuse interface modeling and simulation of surfactants in two-phase fluid flow," *Commun. Comput. Phys.* **14**, 879–915 (2013).
- ³¹H. Diamant and D. Andelman, "Kinetics of surfactant adsorption at fluid-fluid interfaces," *J. Phys. Chem.* **100**, 13732–13742 (1996).
- ³²A. Fakhari and D. Bolster, "Diffuse interface modeling of three-phase contact line dynamics on curved boundaries: A lattice Boltzmann model for large density and viscosity ratios," *J. Comput. Phys.* **334**, 620–638 (2017).
- ³³D. Otis, Jr., E. Ingenito, R. Kamm, and M. Johnson, "Dynamic surface tension of surfactant ta: Experiments and theory," *J. Appl. Physiol.* **77**, 2681–2688 (1994).
- ³⁴G. B. McFadden and A. Wheeler, "On the Gibbs adsorption equation and diffuse interface models," *Proc. R. Soc. London, Ser. A* **458**, 1129–1149 (2002).
- ³⁵D. López-Díaz, I. García-Mateos, and M. M. Velázquez, "Surface properties of mixed monolayers of sulfobetaines and ionic surfactants," *J. Colloid Interface Sci.* **299**, 858–866 (2006).
- ³⁶H. Ju, Y. Jiang, T. Geng, Y. Wang, and C. Zhang, "Equilibrium and dynamic surface tension of quaternary ammonium salts with different hydrocarbon chain length of counterions," *J. Mol. Liq.* **225**, 606–612 (2017).
- ³⁷C.-H. Chang and E. I. Franses, "Adsorption dynamics of surfactants at the air/water interface: A critical review of mathematical models, data, and mechanisms," *Colloids Surf. A* **100**, 1–45 (1995).
- ³⁸A. Fakhari, D. Bolster, and L.-S. Luo, "A weighted multiple-relaxation-time lattice Boltzmann method for multiphase flows and its application to partial coalescence cascades," *J. Comput. Phys.* **341**, 22–43 (2017).
- ³⁹P. L. Bhatnagar, E. P. Gross, and M. Krook, "A model for collision processes in gases. I. Small amplitude processes in charged and neutral one-component systems," *Phys. Rev.* **94**, 511 (1954).
- ⁴⁰T. Krüger, H. Kusumaatmaja, A. Kuzmin, O. Shardt, G. Silva, and E. M. Viggen, *The Lattice Boltzmann Method: Principles and Practice* (Springer, 2016).
- ⁴¹V. M. Kendon, M. E. Cates, I. Pagonabarraga, J.-C. Desplat, and P. Bladon, "Inertial effects in three-dimensional spinodal decomposition of a symmetric binary fluid mixture: A lattice Boltzmann study," *J. Fluid Mech.* **440**, 147–203 (2001).
- ⁴²P.-G. Gennes, F. Brochard-Wyart, D. Quéré *et al.*, *Capillarity and Wetting Phenomena: Drops, Bubbles, Pearls, Waves* (Springer, 2004).
- ⁴³A. J. Wagner, "The origin of spurious velocities in lattice Boltzmann," *Int. J. Mod. Phys. B* **17**, 193–196 (2003).
- ⁴⁴C. Pooley and K. Furtado, "Eliminating spurious velocities in the free-energy lattice Boltzmann method," *Phys. Rev. E* **77**, 046702 (2008).
- ⁴⁵K. Connington and T. Lee, "A review of spurious currents in the lattice Boltzmann method for multiphase flows," *J. Mech. Sci. Technol.* **26**, 3857–3863 (2012).
- ⁴⁶J. Li, Y. Y. Renardy, and M. Renardy, "Numerical simulation of breakup of a viscous drop in simple shear flow through a volume-of-fluid method," *Phys. Fluids* **12**, 269–282 (2000).
- ⁴⁷A. Komrakova, O. Shardt, D. Eskin, and J. Derkens, "Lattice Boltzmann simulations of drop deformation and breakup in shear flow," *Int. J. Multiphase Flow* **59**, 24–43 (2014).
- ⁴⁸G. I. Taylor, "The viscosity of a fluid containing small drops of another fluid," *Proc. R. Soc. London, Ser. A* **138**, 41–48 (1932).
- ⁴⁹G. I. Taylor, "The formation of emulsions in definable fields of flow," *Proc. R. Soc. London, Ser. A* **146**, 501–523 (1934).
- ⁵⁰R. G. van der Sman and S. Van der Graaf, "Emulsion droplet deformation and breakup with lattice Boltzmann model," *Comput. Phys. Commun.* **178**, 492–504 (2008).
- ⁵¹M. Shapira and S. Haber, "Low Reynolds number motion of a droplet in shear flow including wall effects," *Int. J. Multiphase Flow* **16**, 305–321 (1990).
- ⁵²Y. Hu and A. Lips, "Estimating surfactant surface coverage and decomposing its effect on drop deformation," *Phys. Rev. Lett.* **91**, 044501 (2003).
- ⁵³H. Liu, Y. Ba, L. Wu, Z. Li, G. Xi, and Y. Zhang, "A hybrid lattice Boltzmann and finite difference method for droplet dynamics with insoluble surfactants," *J. Fluid Mech.* **837**, 381–412 (2018).
- ⁵⁴F. Huang, Z. Chen, Z. Li, Z. Gao, J. Derkens, and A. Komrakova, "Numerical study of drop behavior in a pore space," *Chem. Eng. Sci.* **233**, 116351 (2020).
- ⁵⁵H. P. Grace, "Dispersion phenomena in high viscosity immiscible fluid systems and application of static mixers as dispersion devices in such systems," *Chem. Eng. Commun.* **14**, 225–277 (1982).
- ⁵⁶A. Kumar, "Isotropic finite-differences," *J. Comput. Phys.* **201**, 109–118 (2004).
- ⁵⁷S. P. Thampi, S. Ansumali, R. Adhikari, and S. Succi, "Isotropic discrete Laplacian operators from lattice hydrodynamics," *J. Comput. Phys.* **234**, 1–7 (2013).
- ⁵⁸Y. Y. Renardy and V. Cristini, "Effect of inertia on drop breakup under shear," *Phys. Fluids* **13**, 7–13 (2001).